1998

A numerical model for the direct steam-heating of municipal solid waste to form carbon slurry feedstock

Steven Quintavalla
Lehigh University

Recommended Citation

Quintavalla, Steven, "A numerical model for the direct steam-heating of municipal solid waste to form carbon slurry feedstock" (1998). *Theses and Dissertations.* Paper 568.

Quintavalla,
Steven

A Numerical Model for the Direct Steam-Heating of Municipal Solid Waste to Form...

January 10, 1999

A Numerical Model for the Direct Steam-Heating of Municipal Solid Waste to Form Carbon Slurry Feedstock

by

Steven Quintavalla

A Thesis

Presented to the Graduate Committee

of Lehigh University

in Candidacy for the Degree of

Master of Science

in

Department of Mechanical Engineering and Mechanics

Lehigh University

Bethlehem, Pennsylvania

November 1998

This thesis is accepted and approved in partial fulfillment of the requirement for the Master of Science.

11/25/98
Date

Prof. Stanley H. Johnson, Ph.D.
Thesis Advisor

Chairman of Department

Acknowledgements

I would like to thank those who have so greatly helped my academic and professional development over the past years. Special thanks to Professor Stanley H. Johnson for his encouragement, his patience, and for allowing me to work on the problem in such a way that I have been able to learn a great deal from it. Finally, thanks to my family, and to my friends for their support and friendship.

Table of Contents

List of Figures

Abstract

A model was developed to characterize the behavior of a packed-bed reactor designed for the steam heating and decomposition of municipal solid waste (MSW). The process described uses direct steam injection to heat newsprint under high pressure. The resulting product is solid carbon in slurry, which is used as a feedstock for a commercial gasifier. The model detailed in this work can be used to examine gas flows in the bed, as well as liquid water movement, vapor-liquid equilibrium, and carbon production from MSW decomposition.

The governing equations were solved using the numerical method of lines approach. The results presented are pressure, temperature, and composition histories of the bed. The spatial distributions of these respective quantities are also presented, at specific points in time. Results are shown for one- and three-dimensional axisymmetric systems.

The results shown indicate that the solution of the equations by this method was successful in simulating the behavior of a packed-bed reactor. Successful simulation required proper numerical treatment, including the use of upwind differences for convected quantities. Numerical accuracy is increased with finer grid definition, although this must be balanced against severe computational demands for three-dimensional problems.

Chapter 1

Introduction

1.1 Background

Useful work on the nature of thermal dispersion and gas movement in finite packed-bed reactors remains largely empirical in nature. Useful correlations have been introduced in the work of Wakao and Kaguei [1]. Intensive numerical treatment of packed-bed systems behavior was investigated in a general sense by Thorsness and Kang, in the context of underground coal gasification [2], [3]. The conservation equations were solved for gas and solid species, as well as energy. In these works, it is noteworthy that Thorsness and Kang chose to model gas velocity using an expression in pressure, derived from the ideal gas law, as opposed to using bed gas distribution.

The first substantial numerical work on the system of concern was undertaken by Thorsness, using ASPEN to model the process dynamically as a lumped unit [4]. This model solved the material and energy balances, without details of the internal spatial variations in the bed. Thorsness later went on to apply a general packed-bed simulator to the problem, resulting in refined projections, including detail on the internal behavior of the system [5]. Again, equations describing conservation of solid and gaseous species and of energy were solved for axisymmetric three-dimensional reactors of various sizes. In this case, gas flows were modeled using bed gas distribution rather than the ideal-gas pressure relationship. Importantly, this work assumed an immobile liquid phase, described as a tractable and useful limiting case. Thorsness approximated vapor-liquid equilibrium using rapid mass transfer between the phases, which was driven by relative concentration differences.

Based on these works, Johnson and Hindmarsh began development of a more specialized code [6] that added detail by allowing for the mobility of the liquid phase, including the filling of external and internal porosities. This model attempted to use a temperature advection term to account for convection energy transport. Finally, the code used an algebraic constraint to account for vapor-liquid equilibrium, as Thorsness did previously. This feature necessitated the use of a differential-algebraic equation solver (DASSL).

1.2 Motivation

This project was undertaken to provide a code specifically developed for the MSW process. Its goals, beyond solving the basic conservation equations, were characterization of the vapor-liquid phase change to include heat effects, proper characterization of steam injection and extraction, and the ability to predict liquid phase flows. To meet these ends, a fast and robust code was developed that will serve as a good platform for future detailed development.

With refined treatments of the thermodynamics involved in the liquid-vapor system and the inclusion of a "headspace" description, this model will serve as the basis for a thorough understanding of the process. The result is the ability to optimize, control, and scale up the system.

1.3 Outline of Thesis

This thesis is divided into three parts: the analytical development of the model, the description of the thermodynamics involved and relationships used, and the method of numerical formulation and solution.

Chapter 2 describes the development of the governing partial and ordinary differential equations that comprise the basis for the model. These equations are basic conservation equations similar to those found in previous work. This chapter also includes the development of an "enthalpy advection" term, similar to the temperature advection description often found in convective heat transfer analysis.

Chapter 3 describes the thermodynamic properties used in the code, including the underlying assumptions of the materials' thermophysical properties. The heat rates associated with the reaction are described, and the model for vapor-liquid heat and mass transfer is detailed.

Chapter 4 describes the method of discretization of the governing equations, including suitable treatment of the convected terms and the boundary conditions. Finally, chapter 5 discusses the results of this work, including relevant conclusions, as well as proposals for future work.

Chapter 2

Development of Governing PDE's

2.1 Solid Species Conversion

The desired process is the conversion of solids, S, the raw material composed of newsprint, to carbon, C, the slurried solid-carbon product. The conversion is modeled as a single irreversible reaction whose chemistry is known. The dynamic behavior of the decomposition is modeled as first-order decay using an Arrhenius constant. The reaction proceeds as follows:

$$S \rightarrow \alpha_C C + \alpha_{NG}(NG) + \alpha_{H_2O}(H_2O) \qquad (2.1)$$

where α_i are the stoichiometric coefficients of the reaction, listed in appendix A. The symbol NG represents the noncondensible gases involved in the process, described and handled in section 2.2. The source rates of the species, s_i, are then:

$$s_i = \alpha_i r_A \qquad (2.2)$$

where the Arrhenius rate r_A is expressed as

$$r_A = \rho_S \cdot A \cdot e^{\frac{-T_a}{T}} \tag{2.3}$$

In these equations, A is the Arrhenius rate constant, and T_a is the activation temperature. The rate is also dependent on the bed density of the solid (ρ_S), expressed in kilograms of solid per cubic meter of bed space.

The solid phases, S and C, are assumed immobile. Therefore, the generation expressions make up ordinary differential equations (ODE's) for these species, which are solved directly. Those generation terms for the gas and liquid species are inserted as source terms into the respective partial differential equations (PDE's).

2.2 Gaseous Species Conservation

Gas species motion is important to the model, in that it serves as the primary mode of heat transfer in the vessel. The Navier-Stokes equation from Bird, Stewart, and Lightfoot [7] is applied after Thorsness [5]:

$$\frac{\partial(\phi c_i)}{\partial t} = -\nabla \cdot (\bar{v}\phi c_i) + s_i + Q_i + \nabla \cdot (CD \cdot \nabla y_i) \tag{2.4}$$

where

c_i = Concentration of gas species i (mol/m^3 of gas space)
C = Total gas concentration
ϕ = Bed porosity (m^3 gas/ m^3 bed)
D = Diffusivity
y_i = Mole fraction of gas species (i) in gaseous mixture
v = Interstitial gas velocity (m/s)
s_i = Source rate of species (i)
Q_i = Rate of introduction of species (i) into the bed

It should be noted that the species introduction term, Q_i, is omitted in the code. Rather, species injection and extraction are handled in the boundary conditions. Excepting the source terms, the right-hand side of this equation is simply the divergence of the species flux:

$$\bar{j}_i = \bar{v}\phi c_i - D(C\nabla y_i) \tag{2.5}$$

and the form of the substantial derivative is recognized. Interstitial velocity is described using Darcy's law [2],

$$\bar{v} = \left(\frac{\Gamma}{\mu}\right)\nabla P \tag{2.6}$$

where

Γ = Bed permeability
μ = Gas dynamic viscosity

P = Pressure

which can be substituted into the conservation expression. This leaves (i) equations for (i) species plus one unknown, pressure. Rather than using an additional equation for total gas conservation, matters are simplified by using an equation of state (chapter 3) to relate pressure to the existing dependent variables: total concentration, C, and temperature, T.

Two gas species are considered in this code. The first is steam, ST, which is modeled as an ideal gas (with properties as described in chapter 4). Besides steam, the remaining part of the gas phase in the physical system is composed of several noncondensible gases, in the initial air in the bed and the gases released from the decomposition reaction. The constituent noncondensible gases include nitrogen, oxygen, and carbon dioxide [4]. For the purpose of simplicity, these components are lumped together as "noncondensible gas", NG. Following the work of Johnson and Hindmarsh, noncondensible gas is represented adequately using the properties of gaseous nitrogen alone.

An important feature is that steam is not generated directly from solid decomposition. Instead, the reaction produces liquid water, which vaporizes as appropriate. Note that vaporization acts as both a source and a sink (condensation) term for steam.

For reasons discussed in Section (4.2), it is desirable that these equations be solved for concentration, in terms of moles of species *i* per unit volume of vapor space. This is as opposed to ϕc_i, which is the concentration in terms of moles per total volume of the bed. This necessitates rewriting the PDE's. Substituting equation (2.5) into equation (2.4), the left-hand side is expanded, which yields...

$$\phi\frac{\partial c_i}{\partial t}+c_i\frac{\partial \phi}{\partial t}=-\nabla\cdot\bar{j}_i+s_i \tag{2.7}$$

rearranging terms,

$$\frac{\partial c_i}{\partial t}=\frac{1}{\phi}\left(-\nabla\cdot\bar{j}_i+s_i-c_i\frac{\partial \phi}{\partial t}\right) \tag{2.8}$$

It becomes necessary to specify an expression for the rate of change of bed porosity. In this context, the bed porosity, ϕ, is defined as the fractional volume of the bed not filled with solids or liquids (though in the next section, this is modified slightly). Thus, taking the time derivative of the free volume:

$$\frac{\partial \phi}{\partial t}=-\frac{1}{MW_{H_2O}\rho_{lw}^0}\frac{\partial c_{lw}}{\partial t}-\frac{1}{\rho_S^0}\frac{\partial \rho_S}{\partial t}-\frac{1}{\rho_C^0}\frac{\partial \rho_C}{\partial t} \tag{2.9}$$

where the solid production rates have been specified. The liquid concentration rate is described in section 2.3.

2.3 Liquid Species Conservation

The convection model for liquid species is of similar form to that of the gaseous species in section 2.2. The single species described is liquid water, a mobile phase with source terms closely related to those for steam. The Navier-Stokes equation is retained from Johnson and Hindmarsh [6]:

$$\frac{\partial c_{lw}}{\partial t} = -\nabla \cdot \left(c_{lw} \bar{v}_{lw}\right) + s_{lw} \tag{2.10}$$

$$\bar{v}_{lw} = \frac{\Gamma_{lw}}{\mu_{lw}} \nabla\left(P - P_c - \rho_{lw} g z\right) \tag{2.11}$$

where those transport coefficients denoted with (lw) are dependent on liquid saturation in the bed (see chapter 4). It will be recognized that liquid flow occurs only after the local interior porosity of the bed is completely filled; that is, water that is held inside the porosity of the paper is not mobile. The source term, s_{lw}, is the sum of the water production rate (via the decomposition reaction) minus the evaporation rate. Movement of the liquid inside the bed is governed by convection only. The driving pressure gradient is different from that in the gas convection expression as static head and capillary pressure are taken into account.

2.4 Conservation of Energy

The final element of the governing model is the equation for conservation of energy. Applying the substantial derivative of the total enthalpy [5]:

$$\frac{\partial\left[\phi\sum_{i}(c_i h_i)+\sum_{k}(\rho_k h_k^{*})\right]}{\partial t}=-\nabla\cdot\left[\sum_{i}(\bar{j}_i h_i)\right]+W+\nabla\cdot(k\nabla T) \qquad (2.12)$$

where

h_i = Gas specific enthalpy (J/mol)
h_k^{*} = Solid/Liquid specific enthalpy (J/kg)
k = Bed thermal conductivity (W/m^2)
W = Local heat source

The flux, j, is described by equation (2.5). The thermal conductivity is described in section (3.1).

The source term, W, arises from the heat of reaction of the decomposition process as well as from the enthalpy of vaporization, thus:

$$W=\sum_{i}s_i h_{f,i}^{0}+s_w\left(h_{f,lw}^{0}-h_{f,st}^{0}\right) \qquad (2.13)$$

where

s_w = Local vaporization rate
$h_{f,i}^0$ = Latent heat of formation at bed temperature (Chapter 4)

Included in the summation is the sink term for the raw material (S), which has a negative value for s_i.

There are two modes of heat transport described here: heat conduction and heat convection. The numerical treatment of these are necessarily different, as explained in section 4.3.2.

2.4.1 Enthalpy Advection

Having found (as described in chapter 4) that the convective terms in the energy equation require different treatment numerically, it was determined that an expression similar to that described as "advection" by Silebi and Schiesser [8] would be desirable. Starting with the basic conservation equation (repeated here for convenience),

$$\frac{\partial\left[\phi\sum_i(c_ih_i)+\sum_k(\rho_kh_k^*)\right]}{\partial t}=-\nabla\cdot\left[\sum_i(\bar{j}_ih_i)\right]+W+\nabla\cdot(k\nabla T) \tag{2.12}$$

the left hand side of the equation is expanded giving

$$\frac{\partial\left[\phi\sum_i (c_i h_i)+\sum_k (\rho_k h_k^*)\right]}{\partial t}=\sum_i\left(\phi c_i\frac{\partial h_i}{\partial t}+\rho_k\frac{\partial h_k^*}{\partial t}\right)+\sum_i\left(h_i\frac{\partial \phi c_i}{\partial t}\right)+\sum_i\left(h_k^*\frac{\partial \rho_k}{\partial t}\right)$$

(2.15)

The first summation represents the rate of change of specific enthalpy of the system. The remaining terms can be referred to as compositional heat changes. Moving these to the right hand side of the equation:

$$\sum_i\left(\phi c_i\frac{\partial h_i}{\partial t}+\rho_k\frac{\partial h_k^*}{\partial t}\right)=-\sum_i\left(h_i\frac{\partial \phi c_i}{\partial t}\right)-\sum_i\left(h_k^*\frac{\partial \rho_k}{\partial t}\right)-\nabla\cdot\left[\sum_i (\bar{j}_i h_i)\right]+W+\nabla\cdot(k\nabla T)$$

(2.16)

Focusing on the first and third terms of the right-hand side, and using substitution of the following expression from equation (2.4),

$$\frac{\partial(\phi c_i)}{\partial t}=-\nabla\cdot\bar{j}_i+s_i \qquad (2.17)$$

these terms simplify to

$$\sum_i \left[\left(h_i \nabla \cdot \bar{j}_i \right) - \nabla \cdot \left(h_i \bar{j}_i \right) \right] + \sum_i h_i s_i \tag{2.18}$$

Finally, the first summation of (2.18) may be manipulated to yield the form

$$\sum_i \left(\bar{j}_i \cdot \nabla h_i \right) \tag{2.19}$$

This defines "enthalpy advection". It is significant that this term encompasses all of the convective and diffusive constituents appearing on both sides of the original energy equation. This is advantageous in that the first-order hyperbolic term has been completely isolated from the parabolic conduction term in the energy equation. As will be discussed in chapter 4, hyperbolic terms require different numerical treatment from parabolic terms.

The remainder of the right-hand side of equation (2.12) is composed of the heat conduction term and the sum of the source terms, represented here:

$$-\sum_i \left(h_i s_i \right) - \sum_i \left(h_k^* \frac{\partial \rho_k}{\partial t} \right) + W \tag{2.20}$$

Recognition that the energy source term, W, is dependent on the same generation rates as the first two terms in this expression leads to one further simplification:

$$Source = \sum_i s_i\left(h_{f,i}^0 - h_i^0\right) + \sum_k s_k\left(h_{f,k}^{*0} - h_k^{*0}\right) \tag{2.21}$$

Finally, combining these terms leads to the temperature equation in its simplest form:

$$\frac{\partial T}{\partial t} = \left[\sum_i\left(\bar{j}_i \cdot \nabla h_i\right) + \sum_l s_l\left(h_{f,l}^0 - h_l^0\right) - \nabla \cdot \left(k \nabla T\right)\right]\left(\phi \sum_i C_{p,i} c_i + \sum_k C_{p,k} \rho_k\right)^{-1} \tag{2.22}$$

where s_l is the generalized source rate of component *l*. The source heat effects may now be considered as rate of heat change due to composition.

2.5 Boundary Conditions

In the gas and liquid conservation PDE's, boundary conditions are set in the same fashion as Thorsness [5]. Boundary conditions are different for walls and injection/extraction areas. Where injection or extraction is present, the flux is specified as a function of injection rate and area. Otherwise, the flux is set to zero. This is the case for the vertical walls of the vessel, as well as some areas of the top and bottom.

The conservation of energy equation requires separate boundary conditions for the various modes of transport. For the conduction mode, a free-convection boundary equation is set [9]:

$$\frac{\partial T}{\partial y} = h_w \frac{T - T_w}{k} \tag{2.23}$$

where

h_w = Wall free convection heat transfer coefficient
T_w = Wall temperature
y = Direction normal to local boundary

Boundary conditions for convective heat transfer are needed only where injection/extraction does not take place (otherwise, j=0 and the wall boundary conditions are in place). Again from Thorsness [5], we find:

$$\sum_i f_i h_i = \sum_i j_i h_i - k\frac{\partial T}{\partial \eta} \tag{2.24}$$

where f_i is the specified injection or extraction flux.

The boundary represented by the centerline is accounted for by the axisymmetric nature of the system; that is, symmetry enforces a zero normal-flux boundary condition along the centerline for each equation. The numerical implications of this are handled in chapter 4.

The solid species governing equations are ODE's and require no boundary conditions.

Chapter 3

Thermodynamic and Physical Relationships

3.1 Thermal Properties

In section (2.2), it was stated that an omission of the conservation of total gas equation leaves an additional unknown, pressure, in the species equations. Consequently, it has become necessary to compute the pressure field by means of an equation of state. For the purposes of simplicity and ease of computation, the ideal gas law was chosen [10]. Therefore, the pressure relationship becomes

$$PV = nRT \tag{3.1}$$

or

$$P = CRT \tag{3.2}$$

where R is the universal gas constant, and all other terms on the right-hand side are known or can be calculated. Therefore, the gaseous species conservation equations are based only on temperature and concentration. Note that the concentration term appears as C (total moles of gas per gas-filled volume), not as ϕC (moles of gas per bed volume). This is because gas pressure depends only on the gas-filled specific volume, not including the solid- and liquid-filled portions of the bed.

By assuming constant heat capacities, the specific enthalpies of the gas species can be simply expressed as [10],

$$h_i = h_i^0 + C_{p,i}(T - 298) \qquad (3.3)$$

where

C_{pi} = Molar heat capacity of gas species (i) (J/mol-K)
h^0_I = Specific enthalpy at reference state (298K)

and the enthalpies of formation are similarly expressed. The advantage of the equations in this form is that deriving the final temperature equation is simplified. In addition, this means that the gas species specific enthalpies are of the same form as those of the liquid and solid species, which is convenient for coding.

The bed conductivity dependence on gas flux [1] is omitted. This property is calculated at every point in the bed, as the volume average of the thermal conductivities of the local constituents.

3.2 Gas Transport Properties

Gas is transported in the bed by two means: convection and diffusion. Diffusion is the simpler of the two, and the sole property to be established is the molecular diffusivity, D. For the purposes of this work, D is assumed constant, and scalar-valued.

Convection in the bed requires the expression of gas viscosity and bed permeability. In the scope of this problem, viscosity is constant-valued, at an intermediate temperature. Permeability is considered scalar-valued and dependent on the degree of bed saturation [6].

$$\Gamma = \Gamma^0 (1 - sat_w)^2,\ 0 \leq sat_w \leq 1 \tag{3.4}$$

where

Γ^0 = Dry bed permeability
sat_w = Fraction of external void filled with liquid

Thus, when the bed is fully saturated, the gas permeability goes to zero, as one would expect. The degree of bed saturation is expressed in terms of the internal and external bed porosity, [6]:

$$\mathrm{v}_s = \frac{\rho_C^0}{\rho_C} + \frac{\rho_S^0}{\rho_S} \tag{3.5}$$

$$\phi_{\mathrm{int}} = \phi_s^0 \frac{\mathrm{v}_s}{1 - \phi_s^0} \tag{3.6}$$

$$\phi_{ext} = 1 - \mathrm{v}_s - \phi_{\mathrm{int}} \tag{3.7}$$

$$sat_w = v_{lw} - \frac{\phi_{\mathrm{int}}}{\phi_{ext}} \tag{3.8}$$

where

v_s = Fractional volume of bed occupied by solids
ρ^0_k = Intrinsic density of solid species (k)
ϕ^0_s = Internal porosity per particle volume fraction

3.3 Liquid Transport Properties

Liquid convection coefficients are similar to those of gas convection. Specifically, liquid viscosity is evaluated at an intermediate temperature and assumed constant. Bed permeability to liquid movement is expressed as

$$\Gamma_{lw} = \Gamma^0 (sat_w)^2 \tag{3.9}$$

which bears direct relation to the gas permeability, equation (3.4).

3.4 Vapor-Liquid Equilibrium

In order to approximate vapor-liquid equilibrium (VLE) for water, an evaporation/condensation rate has been employed that drives the system toward equilibrium. The possibility exists of the use of VLE as an algebraic constraint [6]. This option was not pursued, as it does not allow for the expression of the heat rate of vaporization. The condition for vapor-liquid equilibrium [11]:

$$f_l = f_v \tag{3.10}$$

where f_l and f_v are the liquid and vapor fugacities, respectively. As such, a fugacity difference can be considered as a driving potential [12] for the evaporation rate. Thus:

$$s_w = \kappa K_{mt}\left(f^l - f^v\right) \tag{3.11}$$

Hence, when the liquid fugacity is greater than the vapor fugacity, vaporization occurs, and s_w is positive. When the vapor phase fugacity exceeds the liquid, condensation results, with a corresponding negative value of s_w. In this way, equilibrium is achieved. K_{mt} is a somewhat artificial mass transfer constant, set high enough that equilibrium is achieved rapidly, without computational problems. The term κ is applied to ensure that no more steam or liquid water can be condensed or vaporized than exists locally:

$$\kappa = \begin{cases} \dfrac{c_{lw}^2}{1+c_{lw}^2}, f^l > f^v \\ \dfrac{c_{st}^2}{1+c_{st}^2}, f^l < f^v \end{cases} \tag{3.12}$$

As it is clear that the numerical values for the driving potential can be high (the value of pressure is on the order of 10^5), it is clear that the numerical values for K_{mt} should be low.

As the vapor phase, or steam, has been modeled as an ideal gas, the vapor fugacity is expressed as the local partial pressure of steam. Since the liquid phase is single-component (water), the liquid phase fugacity can be represented by the saturation pressure, P_w, a function of temperature [6], [11]:

$$P_w = P_e \cdot e^{\frac{-a_e}{T}} \tag{3.13}$$

where P_e and a_e are constant within distinct temperature regions (see appendix A).

Chapter 4

Method of Solution

4.1 Method of Lines

This chapter describes the numerical solution of the governing equations and boundary conditions specified in chapter 2, with the embedded relationships in chapter 3. Because this model is made up of PDE's, the solution procedure is the numerical method of lines (NMOL) [13]. The NMOL approach involves the spatial discretization of the PDE's using a method such as finite differences. The result is a large set of ODE's, which are integrated using a numerical integrator. An advantage of this method is the broad availability of robust integrators, which can handle large, stiff systems of ODE's accurately.

4.2 Dependent Variables

The dependent variables for the code are chosen in order to make model computations as straightforward as possible. For example, in the gas conservation equations, the concentration value c_i is solved for since it will be needed directly for the computation of pressure and mole fraction. Similarly, the energy conservation equation is reworked as a temperature equation (chapter 2), as temperature is necessary for the computation of gas pressure, saturation pressure, solid decay rates, and local specific enthalpies.

4.3 Discretization of Spatial Derivatives

Because the geometry is simple, finite differences can be chosen to approximate the spatial derivatives. A cylindrical coordinate system is defined, with the z-axis leading from the top to the bottom of the tank (figure 4.1).

4.3.1 Central Differences

A form of the divergence appears repeatedly in the conservation equations:

$$div = \nabla \cdot \left(A \nabla B \right) \tag{4.1}$$

In cylindrical coordinates, this is expressed as [14]

$$div = \frac{\partial A}{\partial z}\frac{\partial^2 B}{\partial z^2} + \frac{1}{r}\frac{\partial}{\partial r}\left(rA\frac{\partial B}{\partial r} \right) \tag{4.2}$$

where A represents a diffusion property value: diffusivity times concentration , D·C, conductivity, k, or permeability divided by viscosity, Γ/μ, in the respective

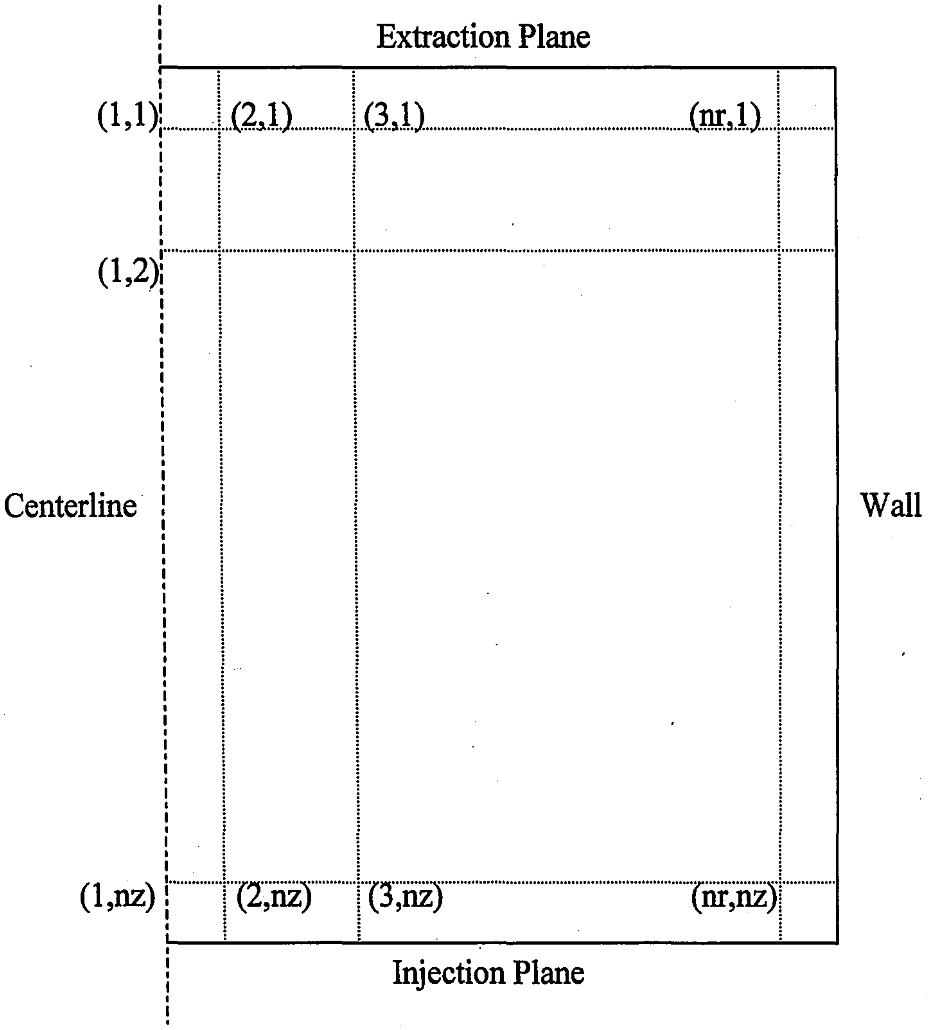

Figure 4.1: Cylindrical Coordinate System

diffusion, conduction, an convection terms. Similarly, B represents driving potential: mole fraction, y_i, temperature, T, or pressure, P, in the same terms. This is convenient, as it allows a single routine to be re-used to compute most of the spatial derivative values.

A convenient centered difference form for the diffusive initial condition problem is found in [15]:

$$(div)_y = \frac{A_{j+1/2} \dfrac{B_{j+1} - B_j}{y_j - y_j} - A_{j-1/2} \dfrac{B_j - B_{j-1}}{y_j - y_{j-1}}}{y_{j+1/2} - y_{j-1/2}} \tag{4.3}$$

where

$$A_j = A(y_j), \ B_j = B(y_j) \qquad \text{(4.4) (4.5)}$$

and y is the generalized spatial coordinate. It is recognized that for the computation of the radial component of the divergence term, the term (A) in the above equation must be replaced by (rA), and the whole term multiplied by (r^{-1}).

4.3.2 Use of Upwind Differences in Advection

The convective terms in the energy equation may be considered as having the characteristics of a first-order hyperbolic PDE, according to Schiesser and Silebi [16].

First-order hyperbolic PDE's are not amenable to the central-difference approximations used in parabolic PDE's, as using central-differences leads to numerical instability. This instability was clearly observed when use of central differences was attempted. Figure (4.2) illustrates the values at a point on the injection plane and at the first grid point interior to that. The unstable, oscillatory behavior demonstrated here is a direct result of the type of discretization used (as described by Patankar [17]) and is not representative of physical reality. This instability is severe enough that it prevents the code from working, and a new approach is required.

One recommended solution to this problem, suggested by Patankar [17], is the use of upwind differencing of the convected quantities. In this solution, while the convective "potential" (the pressure gradient) is computed using a three-point center difference as before, the spatial derivative of the convected quantity is computed using a two-point biased difference. The definition of advection is repeated from chapter 2:

$$Advection = -\sum_i \left(\bar{j}_i \cdot \nabla h_i\right) \qquad (2.19)$$

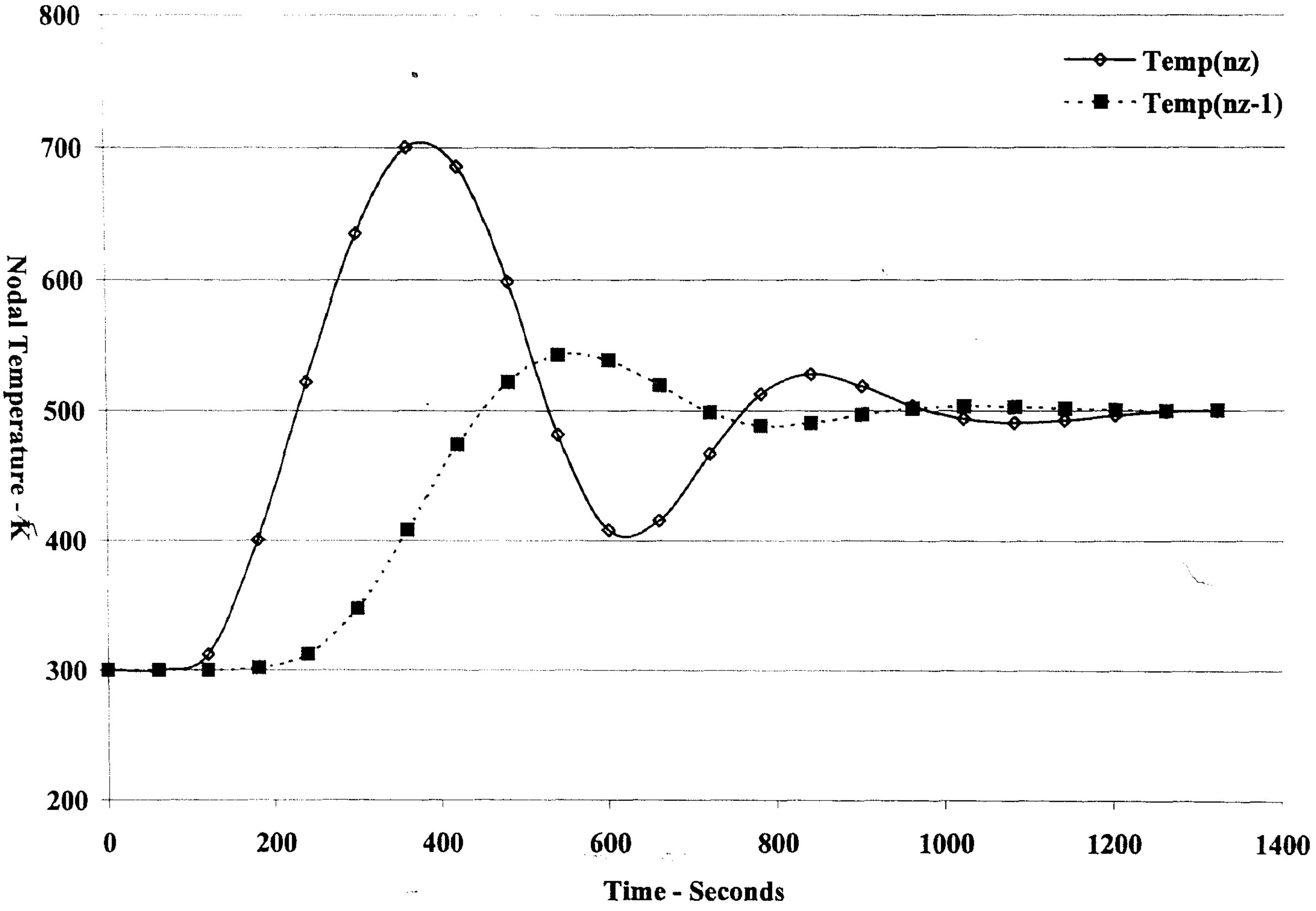

Figure 4.2: Local Injection Temperature Response for Central-Difference Convection Model

For the purpose of illustration, the expression will be simplified, so that a single-species gas convection case can be examined. This is done without loss of generality, because the diffusive component receives the same treatment as the convective transport, and summing the species is a linear operation. The enthalpy advection by convection for a single species is

$$Advection \approx \frac{\Gamma}{\mu} \nabla P \cdot \nabla h \tag{4.6}$$

For the general y-direction, the finite difference form becomes

$$(Advection_y)_j = \begin{cases} \dfrac{\Gamma}{\mu} \dfrac{P_{j+1} - P_{j-1}}{y_{j+1} - y_{j-1}} \dfrac{h_{j+1} - h_j}{y_{j+1} - y_j}, P_{j+1} > P_{j-1} \\ \dfrac{\Gamma}{\mu} \dfrac{P_{j+1} - P_{j-1}}{y_{j+1} - y_{j-1}} \dfrac{h_j - h_{j-1}}{y_j - y_{j-1}}, P_{j+1} < P_{j-1} \end{cases} \tag{4.7}$$

Note that advection in the r- and z- directions are both computed with this equation.

This form is acceptable, so long as the grid is evenly spaced. However, a slight modification of this is needed when the model uses an unevenly spaced mesh. Then, the discretization becomes

$$\left.\frac{\partial P}{\partial y}\right|_j \cong \frac{\frac{\Delta z_{j-1/2}}{\Delta z_{j+1/2}}\Delta P_{j+1/2} + \frac{\Delta z_{j+1/2}}{\Delta z_{j-1/2}}\Delta P_{j-1/2}}{\Delta z_{j+1/2} + \Delta z_{j-1/2}} \tag{4.8}$$

where

$$\Delta X_{j+1/2} = X_{j+1} - X_j \tag{4.9}$$

$$\Delta X_{j-1/2} = X_j - X_{j-1} \tag{4.10}$$

The first derivative is now expressed in a more appropriate form, called divided difference. Using divided differences will become essential as additional solution points are grouped unevenly near the boundaries.

4.4 Expression of Boundary Conditions

Boundary conditions were described for this model analytically in section 2.5. This section discusses the proper numerical treatment for these boundary conditions.

In order to impose the zero-normal-flux boundary condition at the walls (where injection or extraction is not taking place), the normal gradient of the driving potential is set to zero. Using this, the numerical divergence at the outermost grid point *n* becomes

$$Divergence_n = \frac{0-(A)_{n-1/2}\dfrac{B_n - B_{n-1}}{y_n - y_{n-1}}}{y_{n+1} - y_{n-1}} \tag{4.11}$$

where, as in section 4.3.1, (y) represents the general spatial coordinate.

4.4.1 Derivation of Injection/Extraction Boundary Conditions

The original scheme [6] for handling injection and extraction by using source and sink terms was considered unsuitable since it neglected important features of the flux across a boundary. Consequently, discretization of time-variant boundary conditions was desired to model the injection and extraction.

The injection flow rate, Q_i, is specified in moles/second. With this, and equation (2.17), the development proceeds as follows:

$$\frac{\partial \phi c_i}{\partial t} = -\nabla \cdot \bar{j}_i + s_i \tag{2.17}$$

Isolating the flux term on the right-hand side, figure (4.3) shows a control volume drawn above the injection plane. A similar control volume is drawn below the extraction plane. From this:

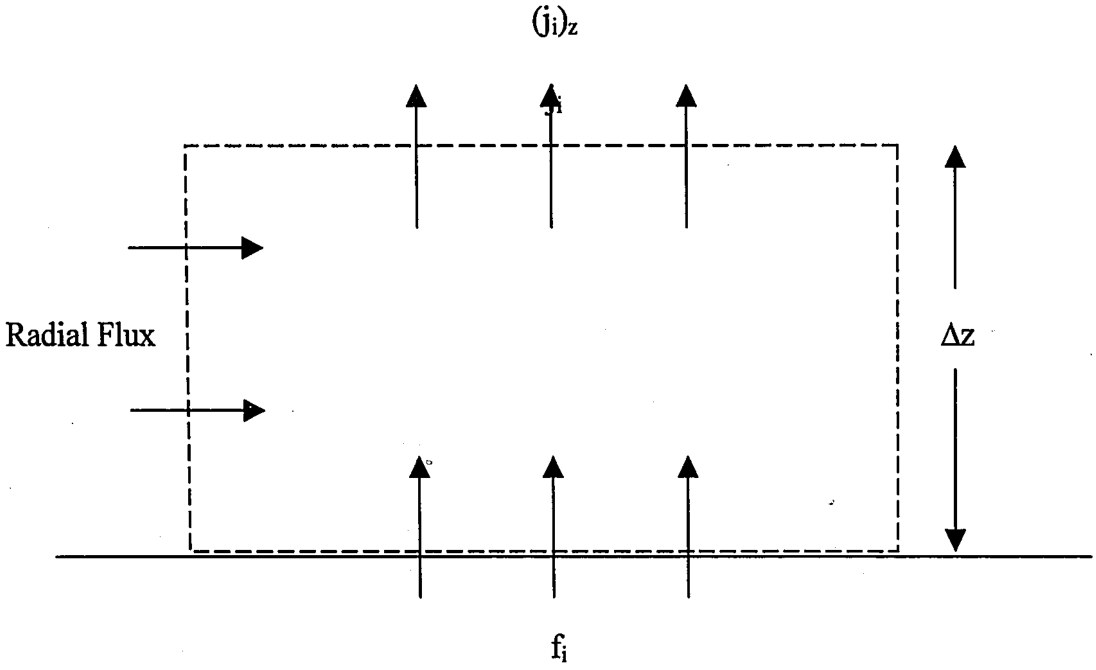

Figure 4.3: Control Volume Above Injection Plane

$$\nabla \cdot \bar{j}_i \cong \frac{(\bar{j}_i)_z - f_i}{\Delta z} + (\nabla \cdot \bar{j}_i)_r \tag{4.12}$$

where f_i is the injection/extraction flux of species *i*, from the specified source rate Q_i:

$$f_i = \frac{Q_i}{A_{inj}} \tag{4.13}$$

The right hand side of equation (4.12) can be separated as:

$$\frac{(\bar{j}_i)_z - f_i}{\Delta z} + (\nabla \cdot \bar{j}_i)_r = \frac{-f_i}{\Delta z} + \frac{(\bar{j}_i)_z - 0}{\Delta z} + (\nabla \cdot \bar{j}_i)_r \tag{4.14}$$

Recognizing that the second term on the right hand side approximates the zero-flux boundary condition, the original equation (2.17) can be rewritten for the wall as

$$\left.\frac{\partial \phi c_i}{\partial t}\right|_{wall} = (-\nabla \cdot \bar{j}_i)_0 + s_i + \frac{Q_i}{A_{inj}\Delta z} \tag{4.15}$$

Therefore, the injection flux at the wall can be included as an artificial source term and added to the rate calculated for zero-gas flux boundaries. Given that the flux must be defined on a discrete number of grid points, the full value of the source term is added only for those points that lie completely within the injection area. For those points that define areas partially outside the injection area, a proportionally lower source rate is defined.

4.4.2 Extraction Algorithm

The extraction flow rate is set to control the maximum pressure at the outlet plane [4]. The result is an extraction function that uses the pressure minus the desired maximum as the driving potential:

$$Q_{ext} = \max\left[\frac{\Gamma}{\mu}\beta(P - P_{\max}), 0\right] \tag{4.16}$$

and the resulting species equations are

$$\left.\frac{\partial \phi c_i}{\partial t}\right|_{wall,ext} = \left(-\nabla \cdot \bar{j}_i\right)_0 + s_i + y_i \frac{Q_{ext}}{A_{inj}\Delta z} \tag{4.17}$$

where the gas mole fraction is included to ensure that the proper proportions of each gas species are removed near the boundary.

The boundary conditions for the enthalpy advection are more straightforward. The flux term is specified, and the enthalpy gradient is computed in a straightforward manner. Where injection occurs

$$\nabla h_i = \frac{h_{i1} - h_{inj}}{z_1 - z_0} \tag{4.18}$$

where the injected gas enthalpy, h_{inj}, is determined from the temperature of the injected gas. Where there is extraction, the enthalpy gradient is set to zero.

4.4.3 Free Convection Heat Transfer

This boundary condition is necessary only for the heat conduction part of the model and is implemented where there is no injection or extraction at the surface. As before, the normal component of the temperature gradient is set to zero at the centerline, in order to preserve the axisymmetric assumption. The numerical implementation of equation (2.23) is similar to that of the zero-flux boundary condition. The difference is that instead of setting the wall derivative to zero, it is set to a value corresponding to the natural convective coefficient at the wall times the temperature difference between the wall and the bed. Using this method, the conduction term at the outermost radial grid point is

$$(Conduction)_{nr} = \frac{(rk)_{nr+1/2}\left(h_{wall}\left(T_{wall} - T_{nr}\right)\right) - (rk)_{nr-1/2}\dfrac{T_{nr} - T_{nr-1}}{r_{nr} - r_{nr-1}}}{r_{nr+1} - r_{nr-1}} \tag{4.19}$$

where, as before, (nr) denotes the outermost radial grid point. It is noted that setting h_{wall} to zero imposes an adiabatic boundary condition.

4.4.4 Centerline Boundary

A complication arises at the centerline, in that the value of radius is zero, so that the expression

$$divergence_r = \frac{1}{r}\frac{\partial}{\partial r}\left(rA\frac{\partial B}{\partial r}\right) \tag{4.20}$$

is undefined. In order to eliminate this difficulty, the term is first expanded,

$$\left.\frac{1}{r}\frac{\partial}{\partial r}\left(rA\frac{\partial B}{\partial r}\right)\right|_{r=0} = \frac{1}{r}\left[rA\frac{\partial^2 B}{\partial r^2} + \frac{\partial A}{\partial r}\frac{\partial B}{\partial r} + A\frac{\partial B}{\partial r}\right] \tag{4.21}$$

recognizing that the first normal derivative of B is set to zero

$$\left.\frac{1}{r}\frac{\partial}{\partial r}\left(rA\frac{\partial B}{\partial r}\right)\right|_{r=0} = A\frac{\partial^2 B}{\partial r^2} + \frac{1}{r}\left[A\frac{\partial B}{\partial r}\right] \tag{4.22}$$

taking the Taylor expansion of the brackets:

$$\left.\frac{1}{r}\frac{\partial}{\partial r}\left(rA\frac{\partial B}{\partial r}\right)\right|_{r=0} = A\frac{\partial^2 B}{\partial r^2} + \frac{A}{r}\left[\left.\frac{\partial B}{\partial r}\right|_{r=0} + r\left.\frac{\partial^2 B}{\partial r^2}\right|_{r=0} + r^2 O(3)\right] \tag{4.23}$$

The first term of the Taylor expansion evaluates to zero, and the third and higher order terms necessarily evaluate to zero at r=0. The remainder is

$$\left.\frac{1}{r}\frac{\partial}{\partial r}\left(rA\frac{\partial B}{\partial r}\right)\right|_{r=0} = 2A\frac{\partial^2 B}{\partial r^2} \tag{4.24}$$

which is approximated easily with a three-point centered difference [15].

4.5 Initial Conditions

It is desirable for the initial conditions to be specified in a consistent manner. The volume of the vessel is set, and the amount of solid reactant and water are specified at desired levels. So, too, are the initial pressure and temperature specified. To ensure that the integration is properly started at steady-state, the amounts of noncondensible gas and steam must be established using vapor-liquid equilibrium. Typical startup values for a pilot-scale reactor 1 meter in height and 1.3 meters in diameter are

Quantity	**Symbol**	**Initial Value**
Pressure	P	10^5 Pa
Temperature	T	300 K
Solids Mass	M_S	189 kg
Water Mass	M_W	90 kg

These are all the parameters that are needed to specify the initial state of the system.

From the vessel volume and initial masses,

$$\rho_S = \frac{M_S}{V_{bed}} \qquad C_W = \frac{M_W}{V_{bed}} \tag{4.25) (4.26}$$

$$\phi = 1 - \frac{\rho_S}{\rho_S^0} \tag{4.27}$$

The saturation pressure can be calculated from the initial system temperature using equation (3.12). To ensure phase equilibrium,

$$c_{st} = \frac{P^w}{RT} \tag{4.28}$$

then:

$$c_{lw} = \frac{(C_W - \phi c_{st})}{1 - c_{st}\dfrac{MW_{H_2O}}{\rho_{lw}^0}} \qquad c_{ng} = \frac{P}{RT} - c_{st} \tag{4.29) (4.30}$$

4.6 Solution of Governing Equations

The integration of the governing equations was accomplished using DASSL (Differential/Algebraic System Solver) [18]. Though the initial VLE model, which resulted in a differential/algebraic equation (DAE) set no longer exists, DASSL was retained as the solver. This is so because DASSL is able to integrate the equations reliably and gives the code increased flexibility for future development.

The code integrates the equations for a specified length of time (typically six hours). Results are presented in terms of pressure, temperature, vapor phase composition, liquid water volume, injection, extraction, and bed densities of solid and carbon. Output is in the form of continuously reported vessel volume averaged data, as well as discrete instances of full spatial data.

Chapter 5

Results and Discussion

5.1 Simulations

In order to illustrate the capabilities of the code developed from the model described in this work, the results from three simulations are presented. Results were obtained using a Pentium computer with 233 MHz processor speed. Studies were run for

- Uniform flux (one-dimensional case)
- Core injection/extraction (three-dimensional axisymmetric)
- Core injection/extraction with refined mesh

The first results shown are for the simplest case of uniform injection and extraction. The second study illustrates the model's ability to handle two-dimensional spatial variations. Finally, the second study was re-run with a denser grid spacing to investigate the model's mesh sensitivity.

The initial conditions and vessel dimensions were the same for all studies. A list of the physical parameters used in the model is found in appendix A, and are primarily published data [9], [10]. In each simulation, the same injection rate (moles/second) and steam temperature are used on the process to provide a consistent basis for comparison. The steam injection strategy can be found in figure (5.1). This is essentially the same strategy used for the pilot scale reactor described by Thorsness [5], but with lower maximum values.

The simulated time in each case was six hours. The first two simulations were performed using eight vertical and six radial locations, for a total of forty-eight grid points. Comparative computational performance indicators for these cases are listed in appendix B.

5.1.1 Uniform Boundary Flux (one-dimensional Results):

This simplest simulation was the first completed and was used to determine whether the model behaves in a physically realistic manner. Figure (5.1) displays the injection and extraction over the first four hours of simulation. Note from section 4.4.2 that the extraction algorithm was chosen to maintain a maximum pressure (6 x 10^5 Pascals) at the top of the vessel. The resulting extraction, after an initial transient, tracks the injection level. It does so at a much higher rate initially, reflecting the fact that liquid is being evaporated even as the steam is injected. As the bed substantially dries out, the extraction follows the injection more closely.

The pressure history, in figure (5.2), shows the same initial excess gas from vaporization. The mean bed pressure is highest during the initial stage of injection

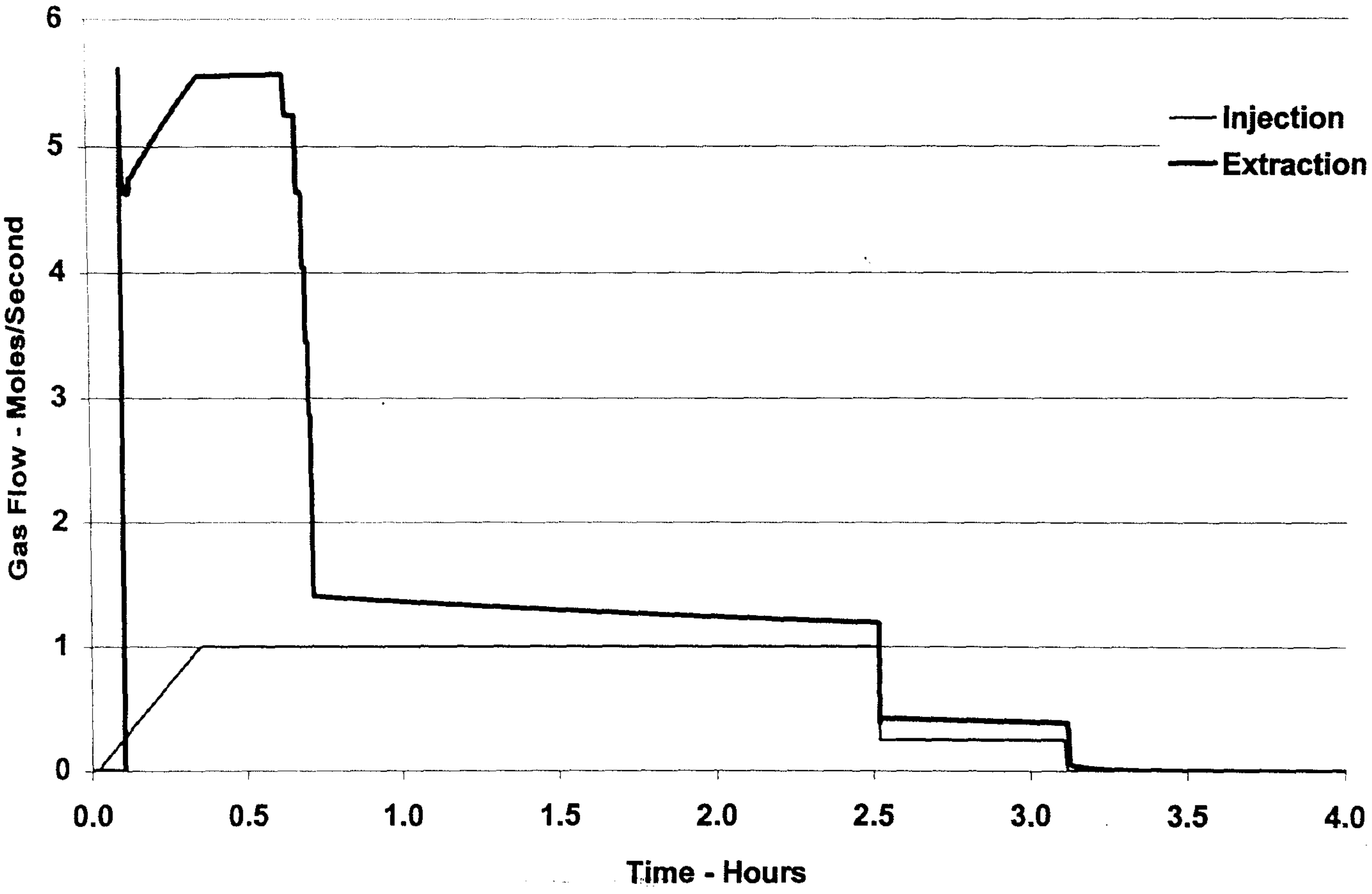

Figure 5.1: Steam Injection/Gas Extraction vs. Time (Uniform Flux)

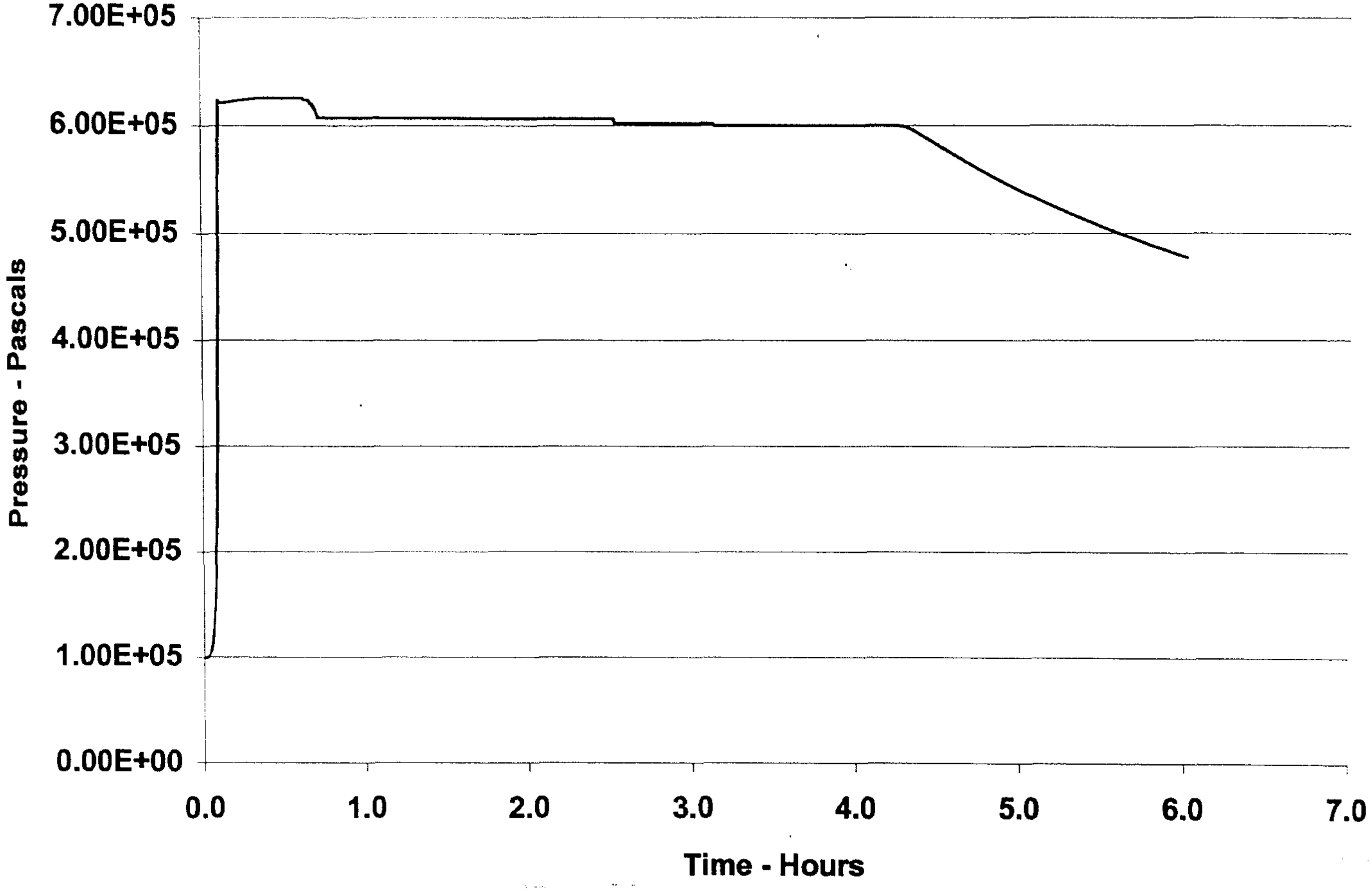

Figure 5.2: Pressure vs. Time (Uniform Flux)

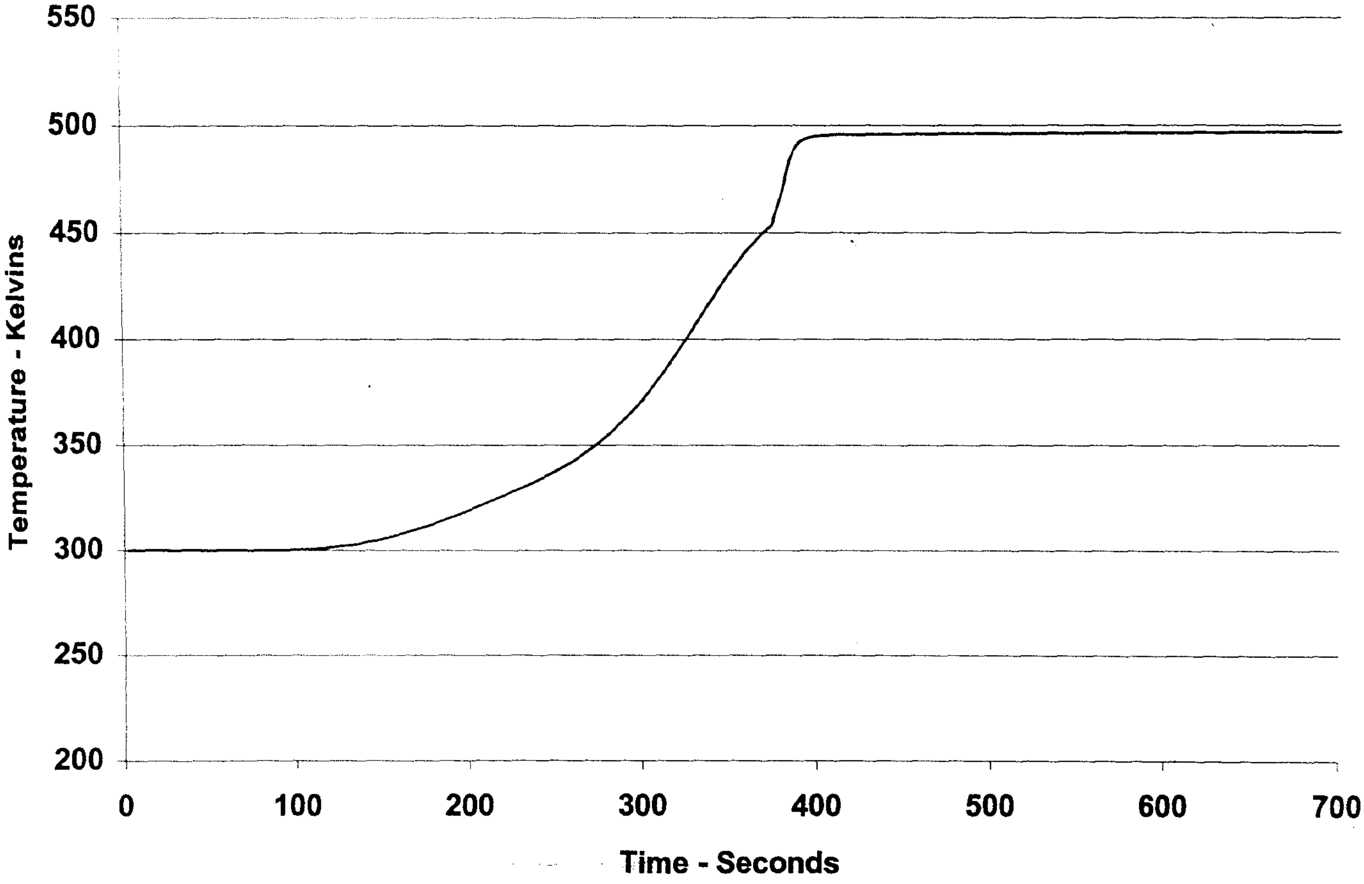

Figure 5.3: Start-up Temperature (Uniform Flux)

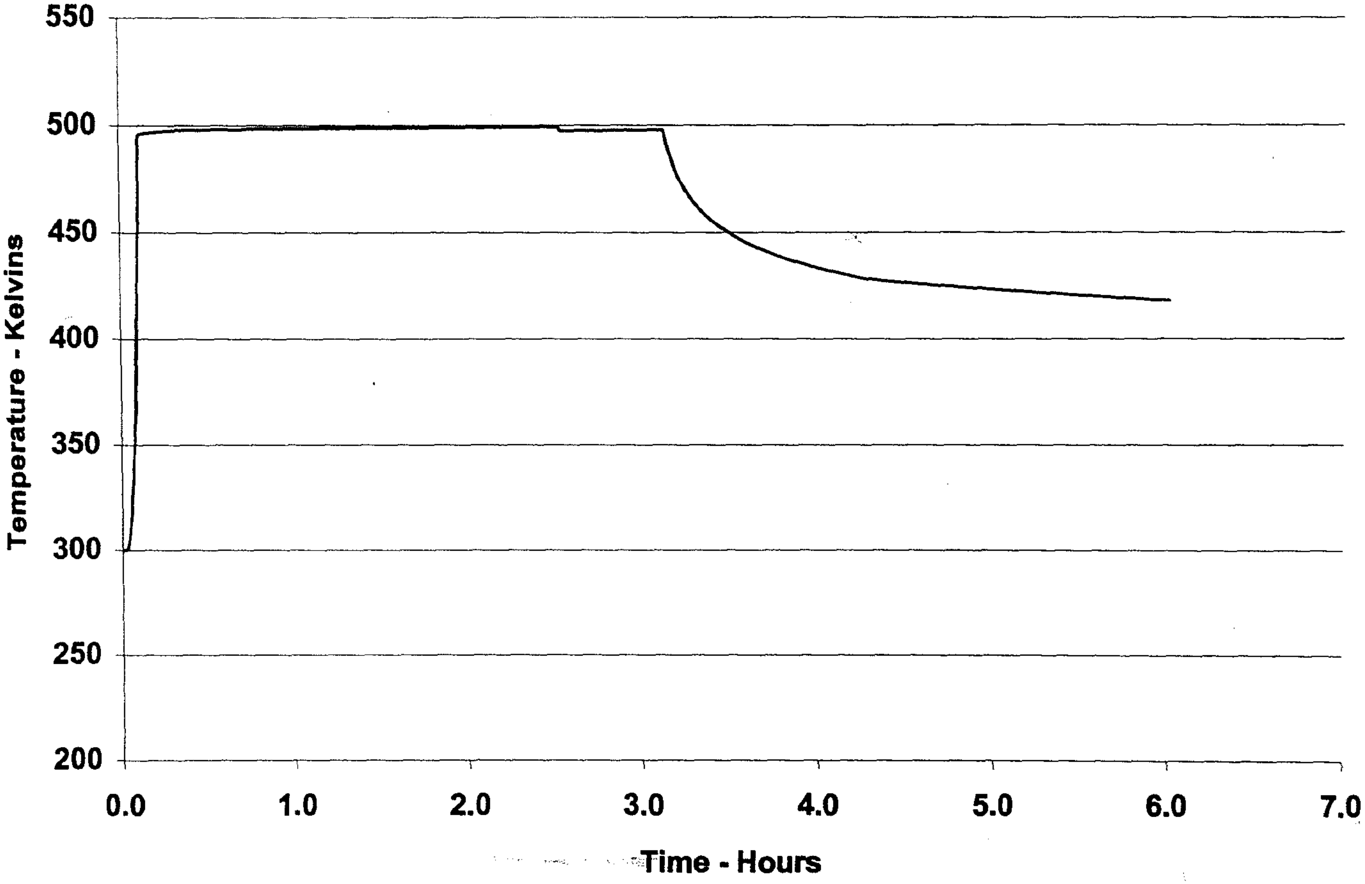

Figure 5.4: Temperature vs. Time (Uniform Flux)

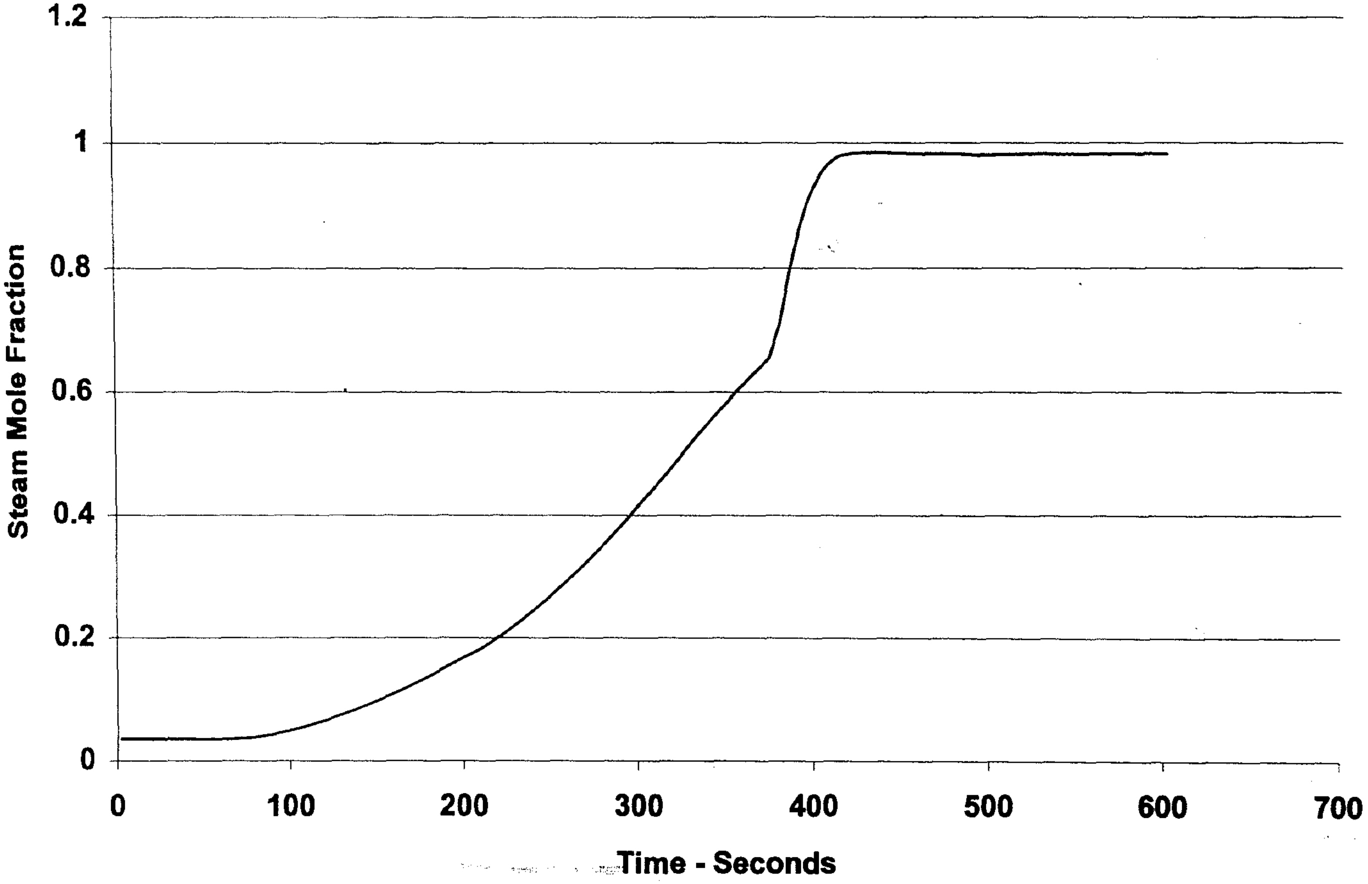

Figure 5.5: Start-up Bed Gas Composition (Uniform Flux)

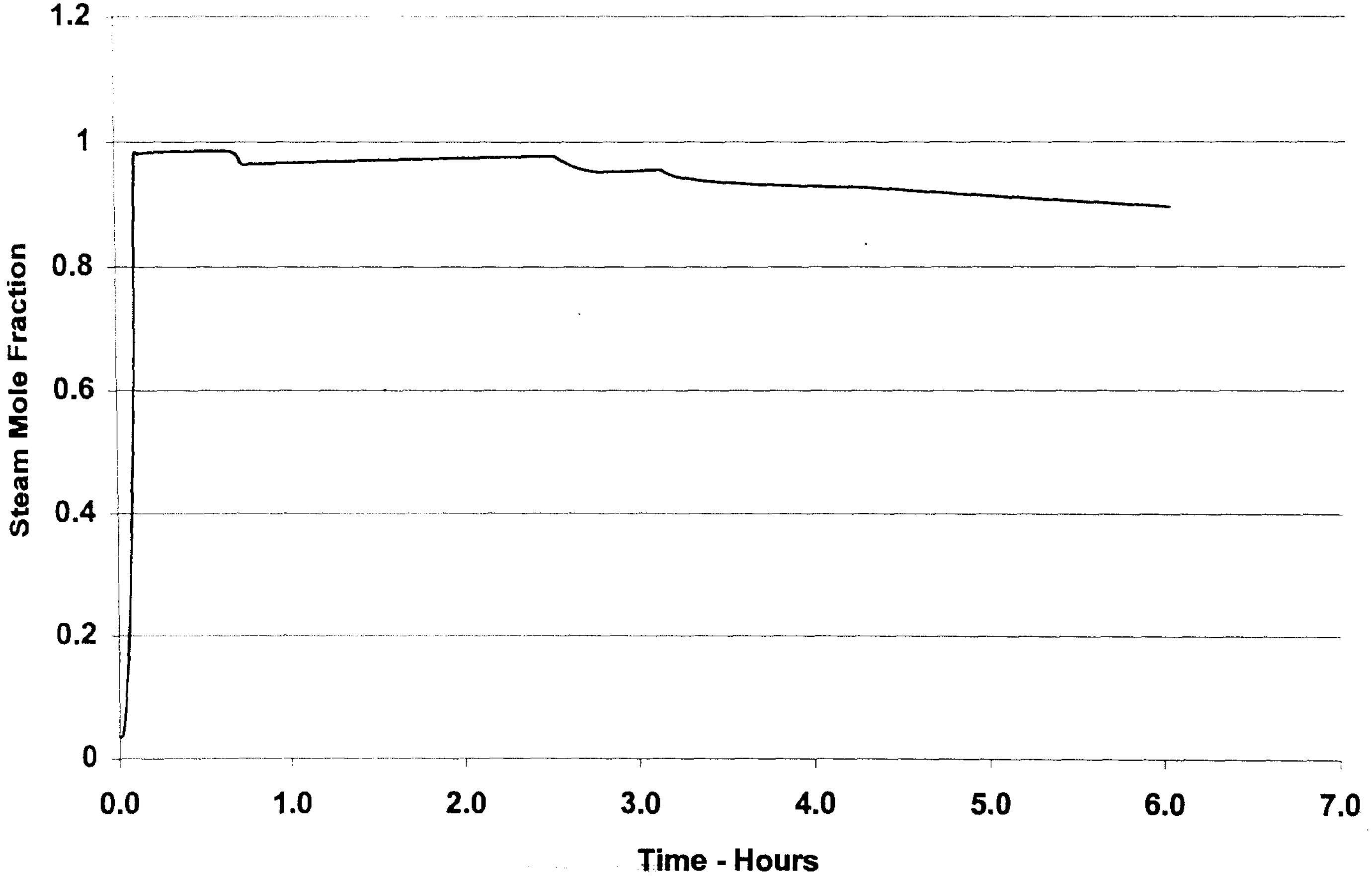

Figure 5.6: Bed Gas Composition vs. Time (Uniform Flux)

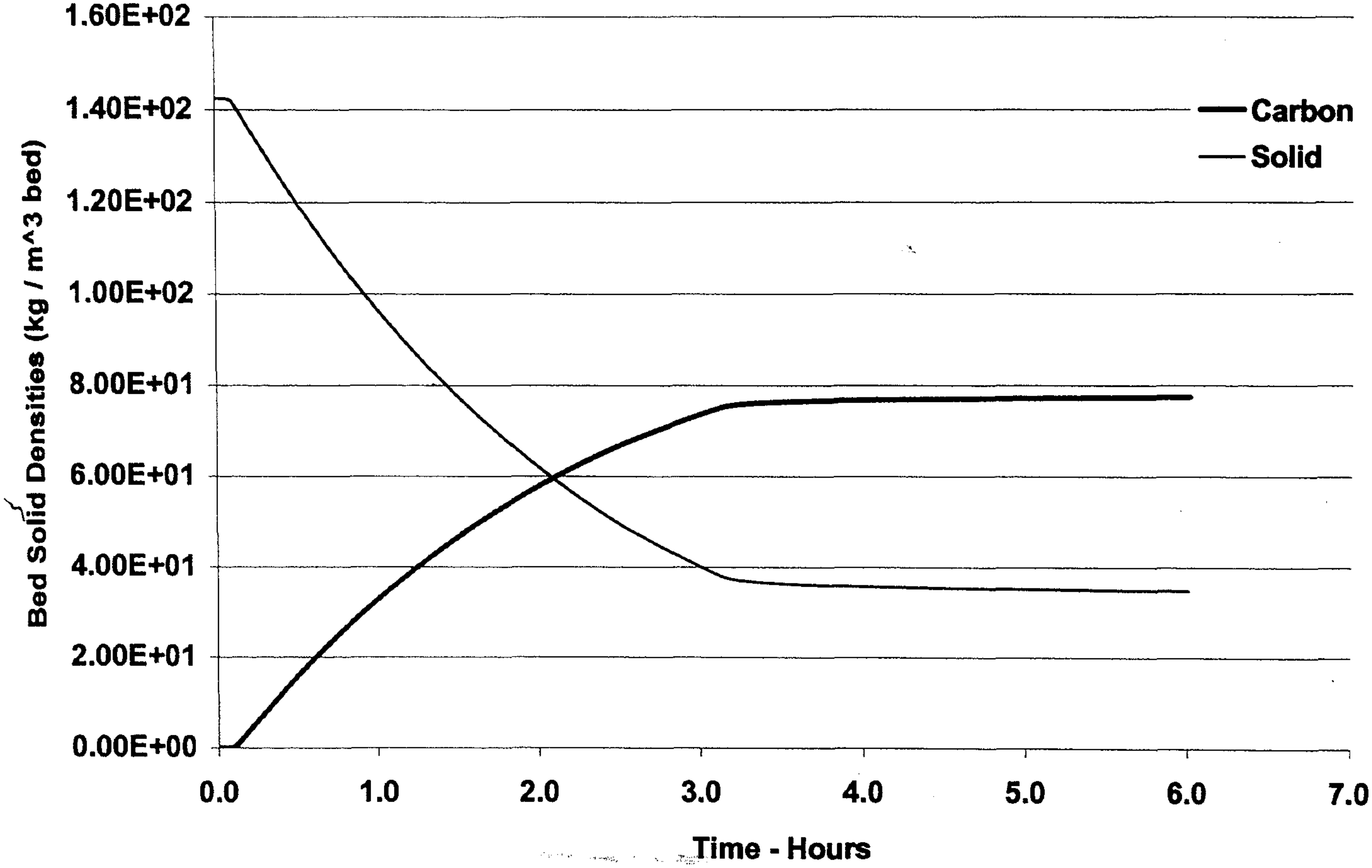

Figure 5.7 - Bed Solids Composition (Uniform Flux)

and drying. While injection is taking place, the average pressure in the vessel is. expectedly higher than the controlled pressure at the top. After 11160 seconds, the pressure is maintained at the same level until reaction-related cooling of the bed causes a pressure decline.

The temperature history during initial start-up, in figure (5.3), exhibits a knee at the point where extraction begins. It is at that point that cooler gases that have collected at the top of the bed are drawn off, and the bed temperature reaches equilibrium near the injection temperature more quickly. The long-term temperature history, illustrated in figure (5.4), demonstrates behavior similar to the pressure history. It is clear that temperature drops off right after the second injection phase is completed. At this point, extraction continues, and pressure gradients still exist, which explains the fact that temperature drops earlier than pressure in these results.

The bed gas composition is modeled using the steam mole fraction. A similar behavior to the initial temperature profile is seen in the transient steam mole fraction in figure (5.5). At the extraction beginning point, the noncondensibles at the top are evacuated, leading to a faster steam saturation of the bed. The longer-term gas composition history, in figure (5.6), demonstrates noncondensible production as well as some condensation after injection has stopped and the bed cools.

Figure (5.7) represents the focus of the process -- the conversion of solids to carbon. It is evident that in this case, the amount of carbon product has exceeded the solid reactant and that as temperatures decline, so does the rate of conversion.

5.1.2 Core Boundary Flux (Three-dimensional Axisymmetric Results):

Figure (5.8) shows extraction behavior similar to that of the one-dimensional system, except that the initial extraction rate is not as high. This is not surprising when figure (5.11) is examined, and it is seen that the temperature does not increase as quickly or to as large a magnitude (this will be apparent when the bed property contours are explored). The pressure history, in figure (5.9), follows the injection profile in a similar fashion to the one-dimensional case, though bed pressure after injection drops off more quickly.

The temperature and steam mole fraction transients, figures (5.10) and (5.12), exhibit a knee at the extraction start as before, if less pronouncedly. In fact, it is only a few seconds after the extraction start that the temperature increase seems to continue at a lower rate. As the mean temperatures in the bed are, on the whole, lower than in the uniform flux scenario, it is no surprise that the rate of conversion of solid to carbon is much lower. In fact, as illustrated in figure (5.14), the level of carbon product does not reach that of reactant by the end of six hours. It should be kept in mind that the injection rates involved in this work are only half those described by Thorsness [5].

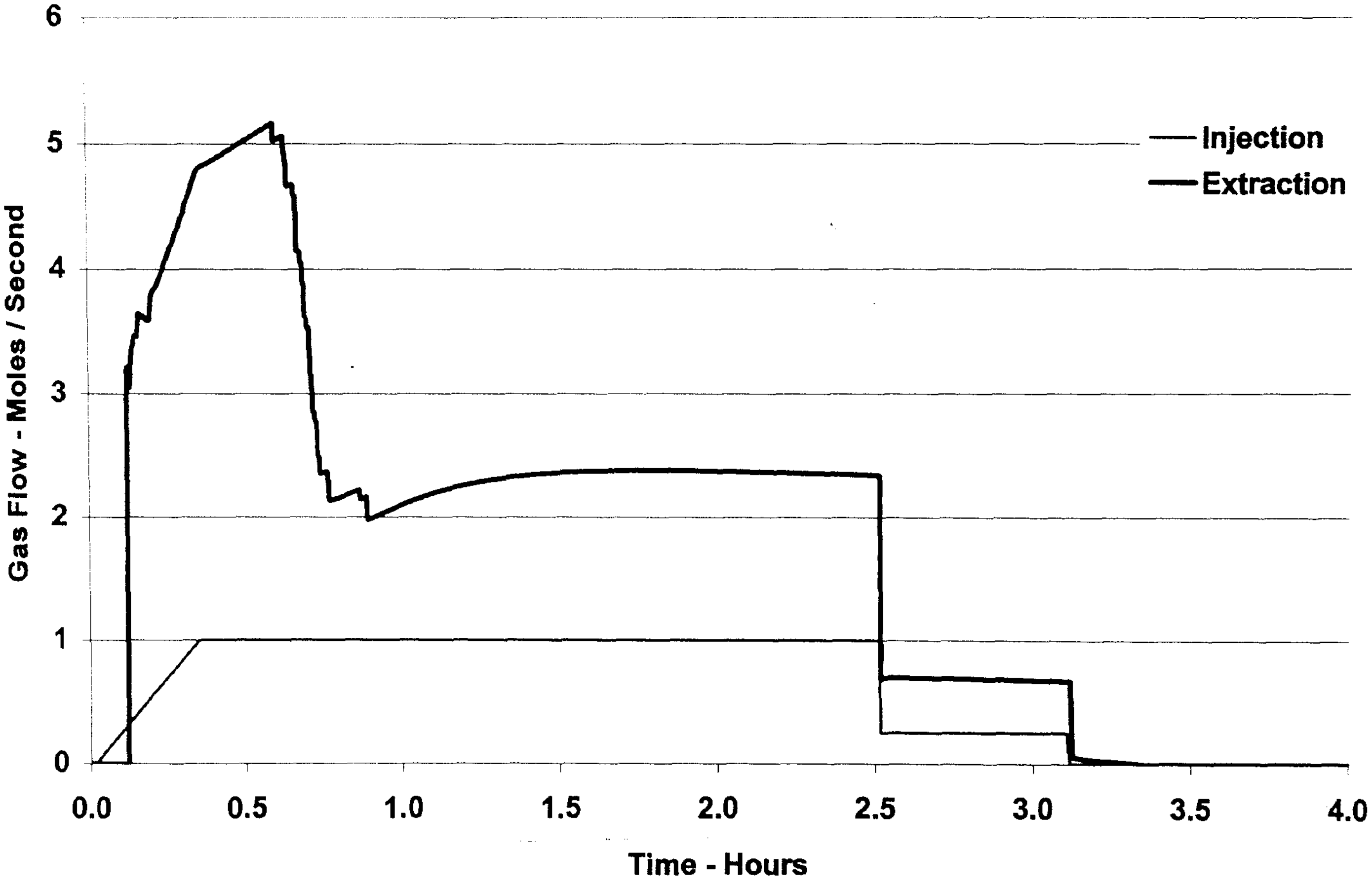

Figure 5.8: Steam Injection/Gas Extraction vs. Time (Core Flux)

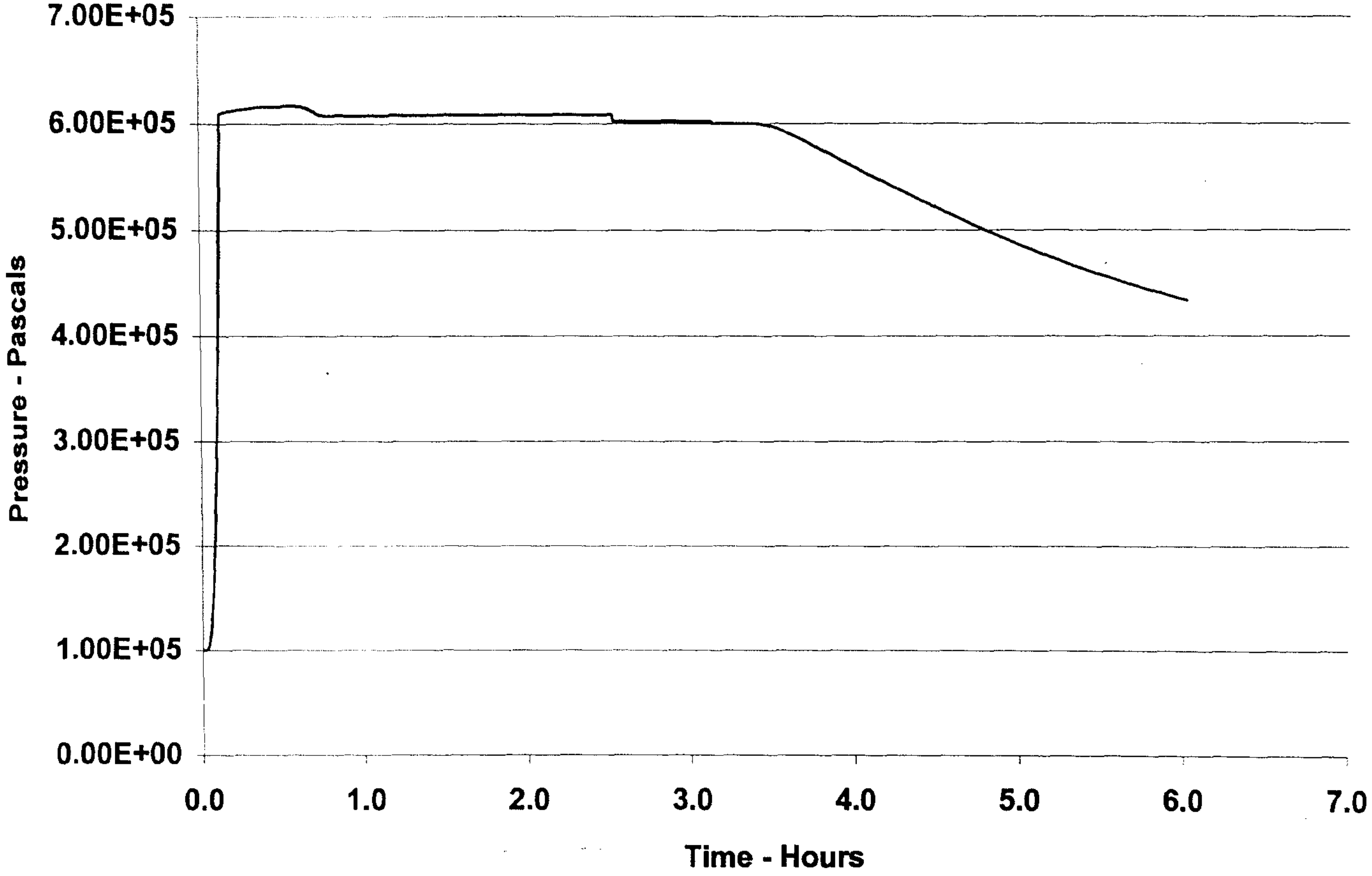

Figure 5.9: Pressure vs. Time (Core Flux)

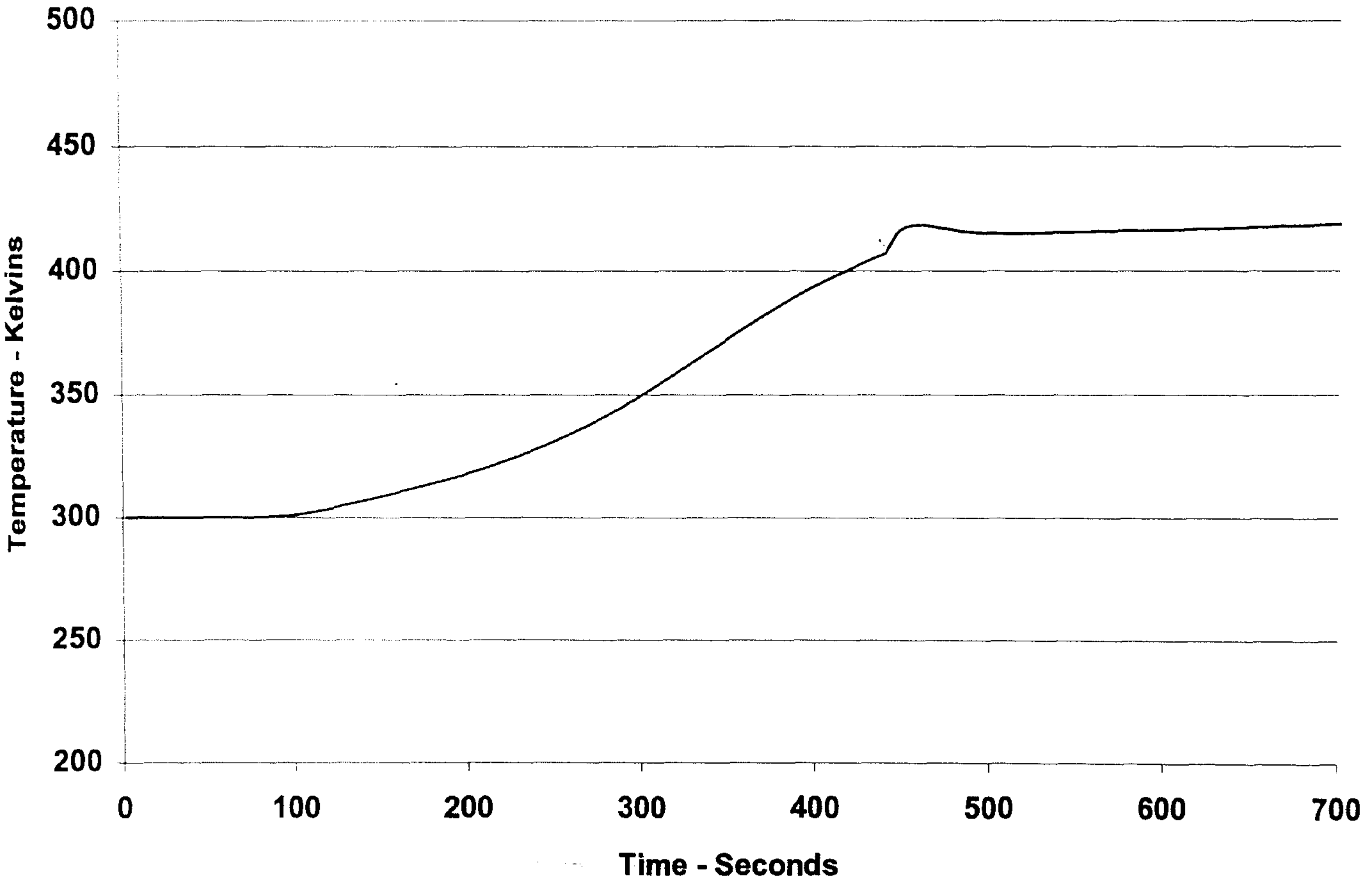

Figure 5.10: Start-up Temperature (Core Flux)

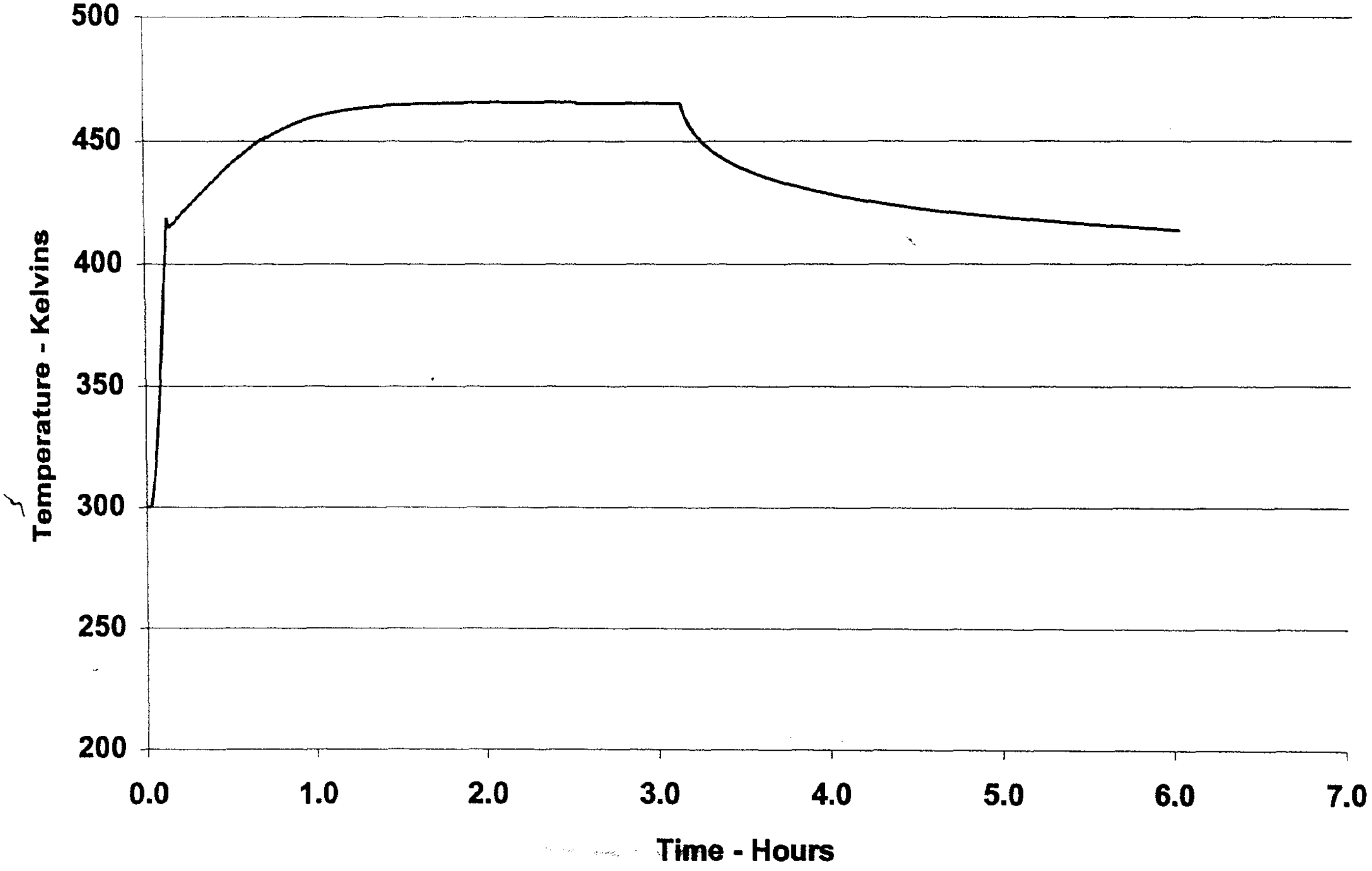

Figure 5.11: Temperature vs. Time (Core Flux)

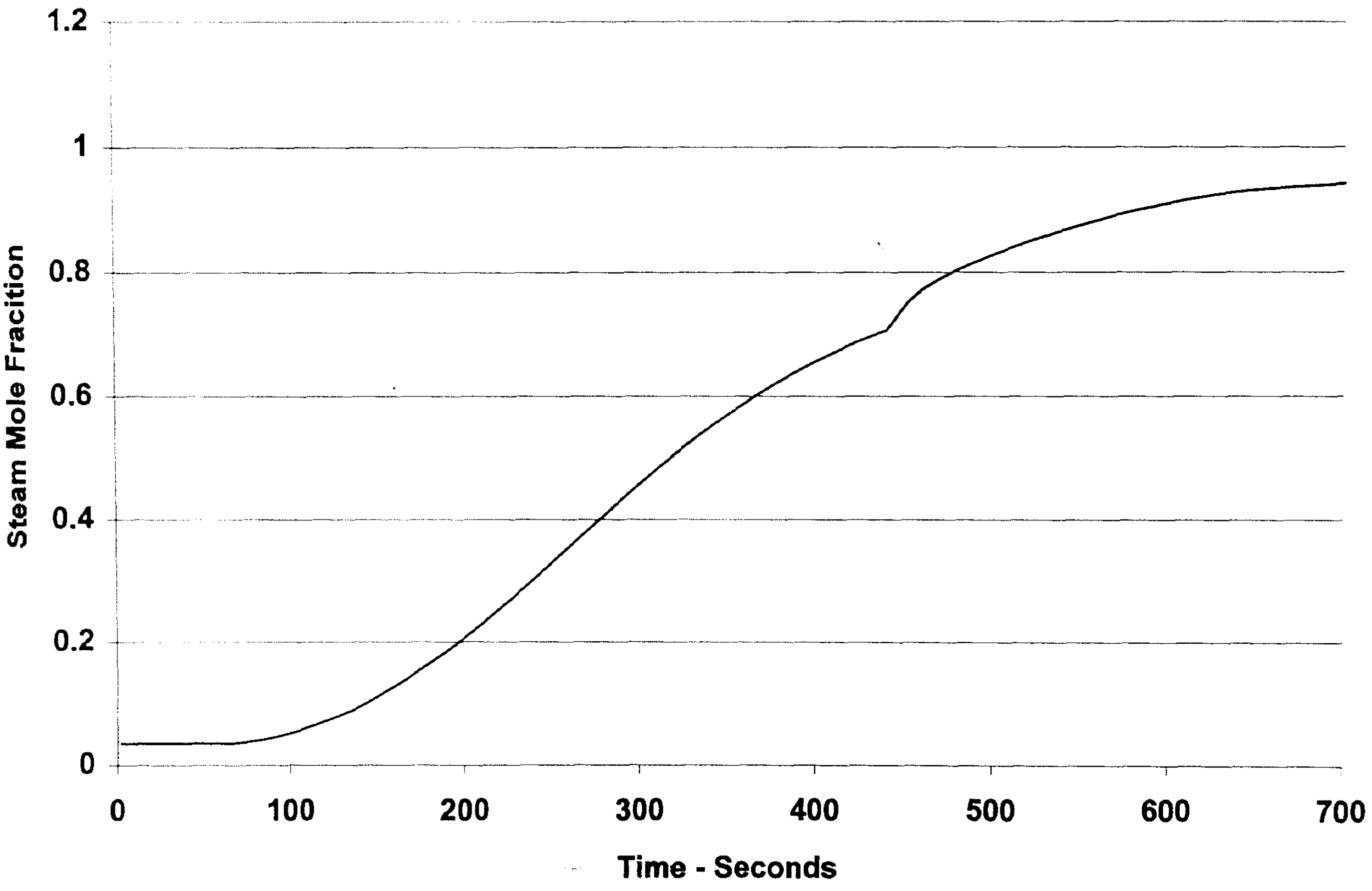

Figure 5.12: Start-up Gas Composition (Core Flux)

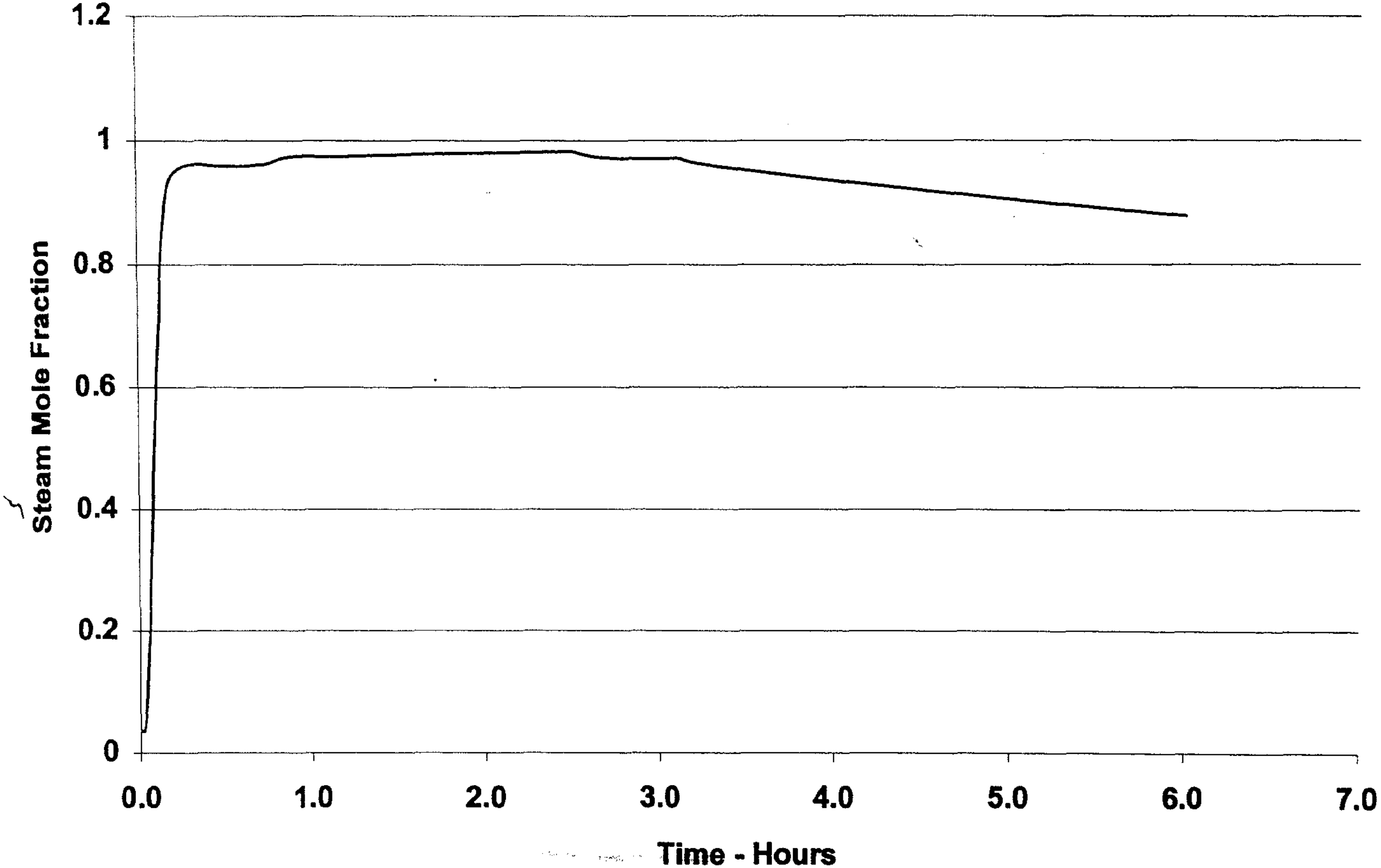

Figure 5.13: Gas Composition vs. Time (Core Flux)

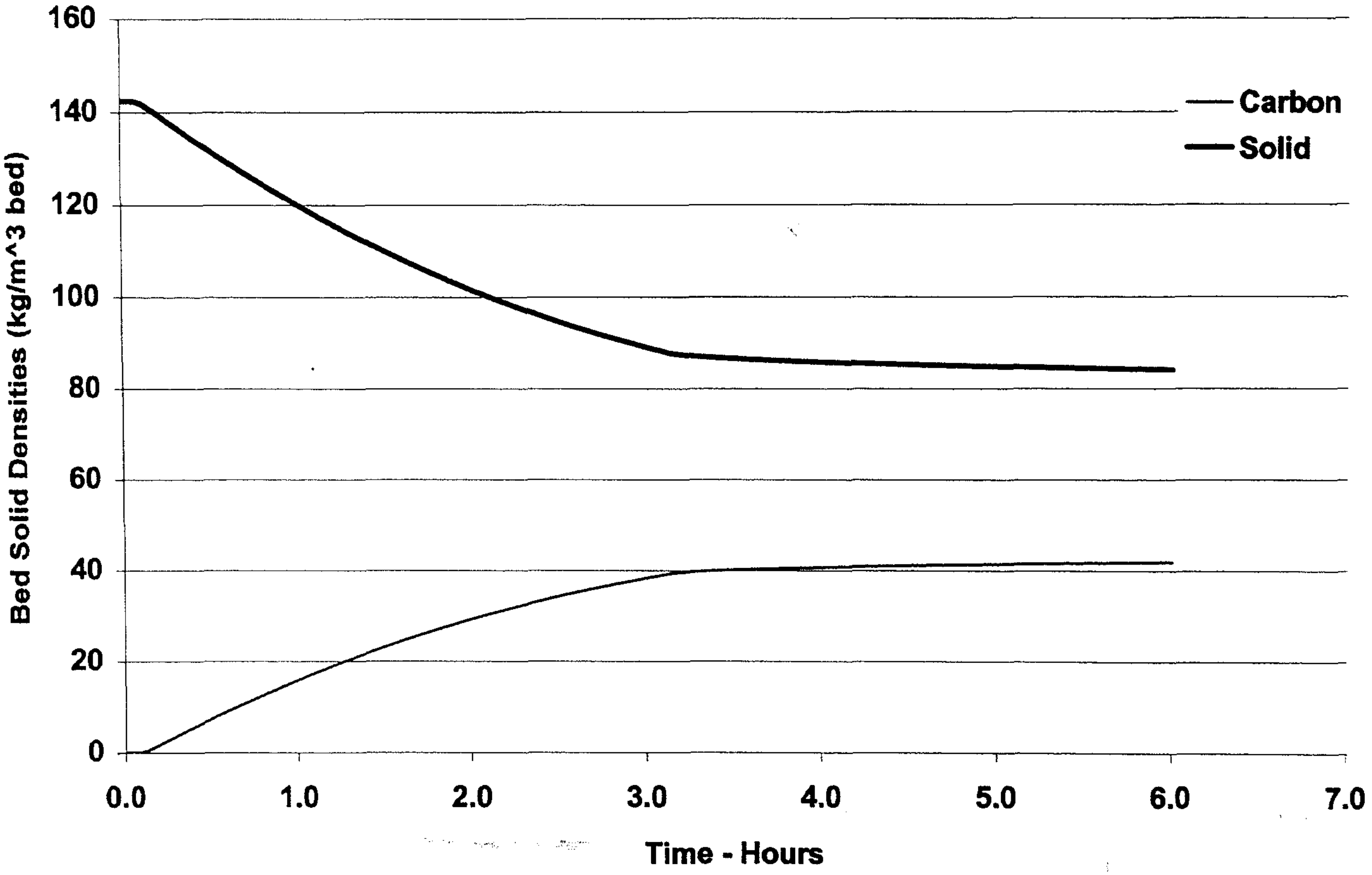

Figure 5.14: Bed Solid Composition vs. Time (Core Flux)

The differences between the two cases may be explained by examination of the contour plots of the internal bed behavior. Figures (5.15), (5.16), (5.17), and (5.18), respectively, illustrate the state of the reactor at 300 seconds (during the initial transient), 1200 seconds (first extraction), 9000 seconds (at the end of full injection), and 12000 seconds (end of extraction).

At the 300-second mark, the bed behavior is as might be expected. There is a gradual pressure gradient and well-defined temperature and steam fronts. It is already quite clear that the zero-flux, adiabatic walls are inhibiting heat transfer to the outermost annulus of the vessel. The 1200-second behavior clearly shows that this has remained so. The pressure field at this time shows the effect of extraction at the core, where it is remembered that gas velocity runs perpendicular to lines of constant pressure.

By 9000 seconds, the contents of the entire vessel have heated (in part due to conduction), though the contents of the outer vessel are still significantly cooler than the core. At this point, it should be remembered that the outer radius of the vessel holds more of the volume, which explains why the average temperature is not closer to the 500K found over much of the volume.

At 12000 seconds, the pressure gradients have dissipated, and gas moves by diffusion. There is a higher core temperature still evident, one that will be dissipated by conduction and the energy consumed in the decomposition reaction.

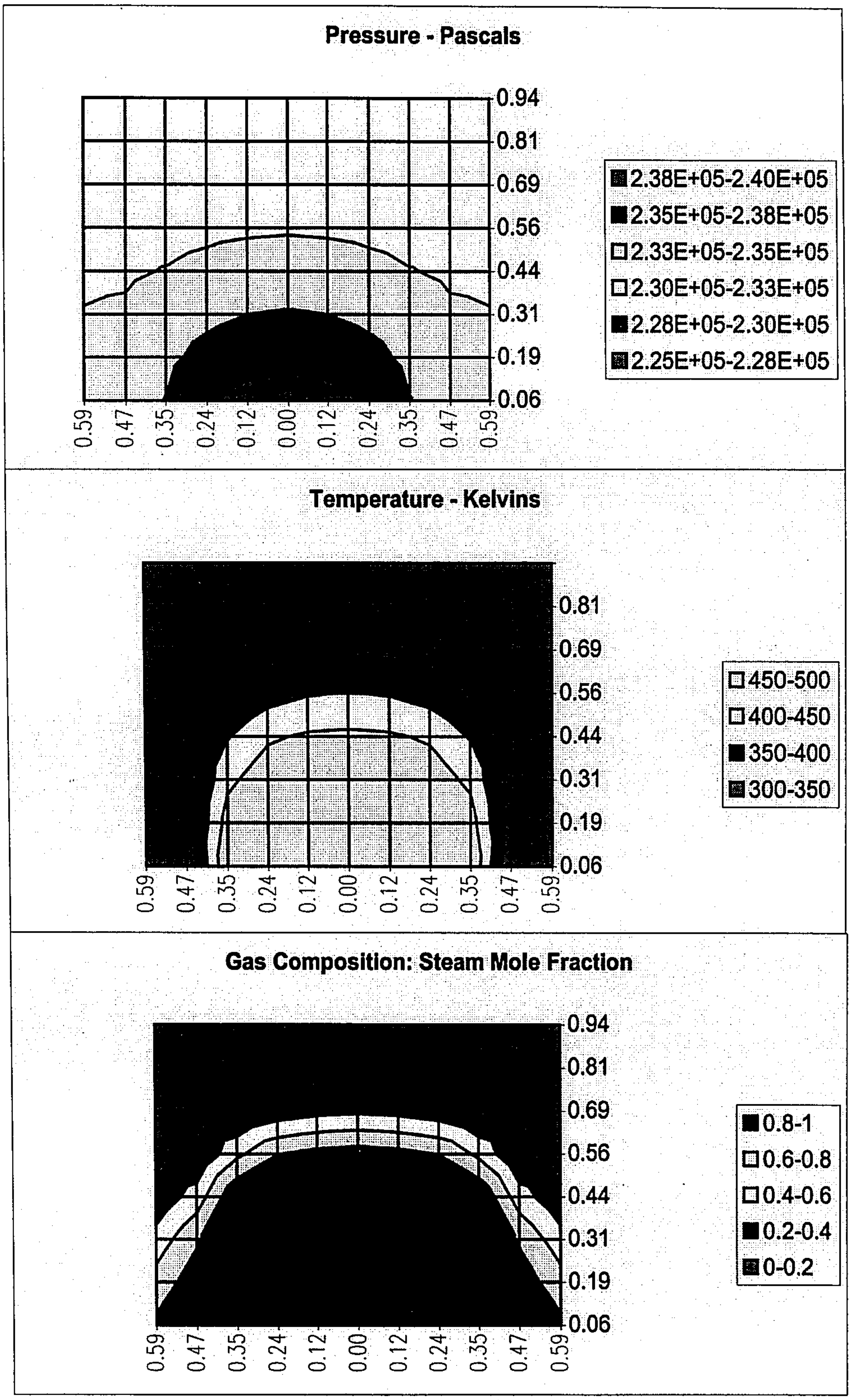
Pressure - Pascals

Temperature - Kelvins

Gas Composition: Steam Mole Fraction

Figure 5.15: Spatial Contours, 300 seconds.

Pressure - Pascals

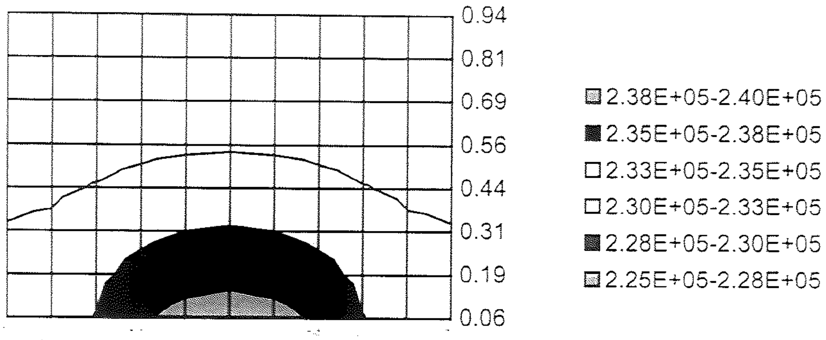

Temperature - Kelvins

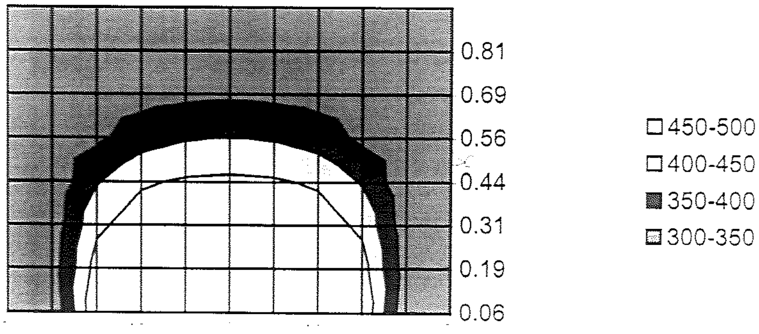

Gas Composition: Steam Mole Fraction

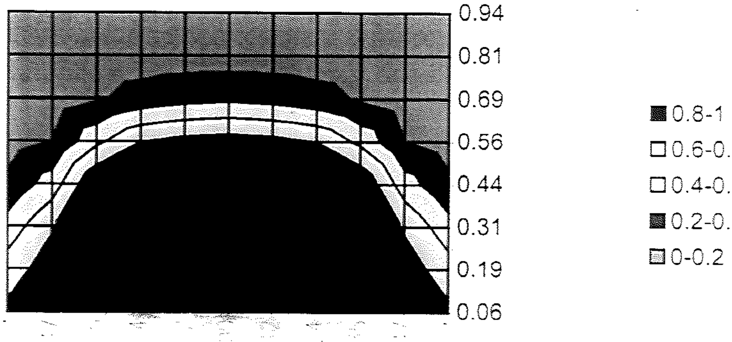

Figure 5.15: Spatial Contours, 300 seconds.

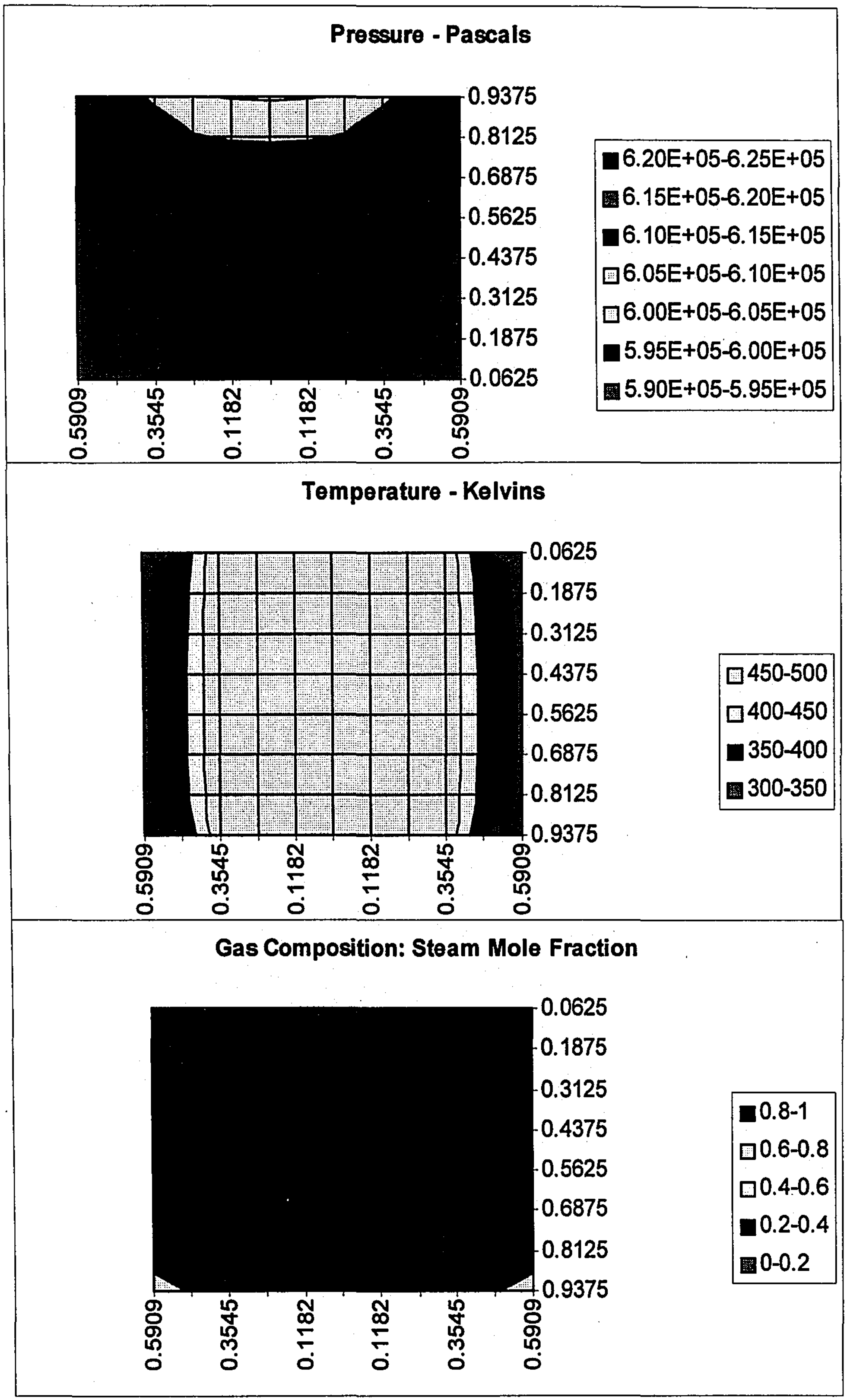
Pressure - Pascals

Temperature - Kelvins

Gas Composition: Steam Mole Fraction

Figure 5.16: Spatial Contours, 1200 seconds.

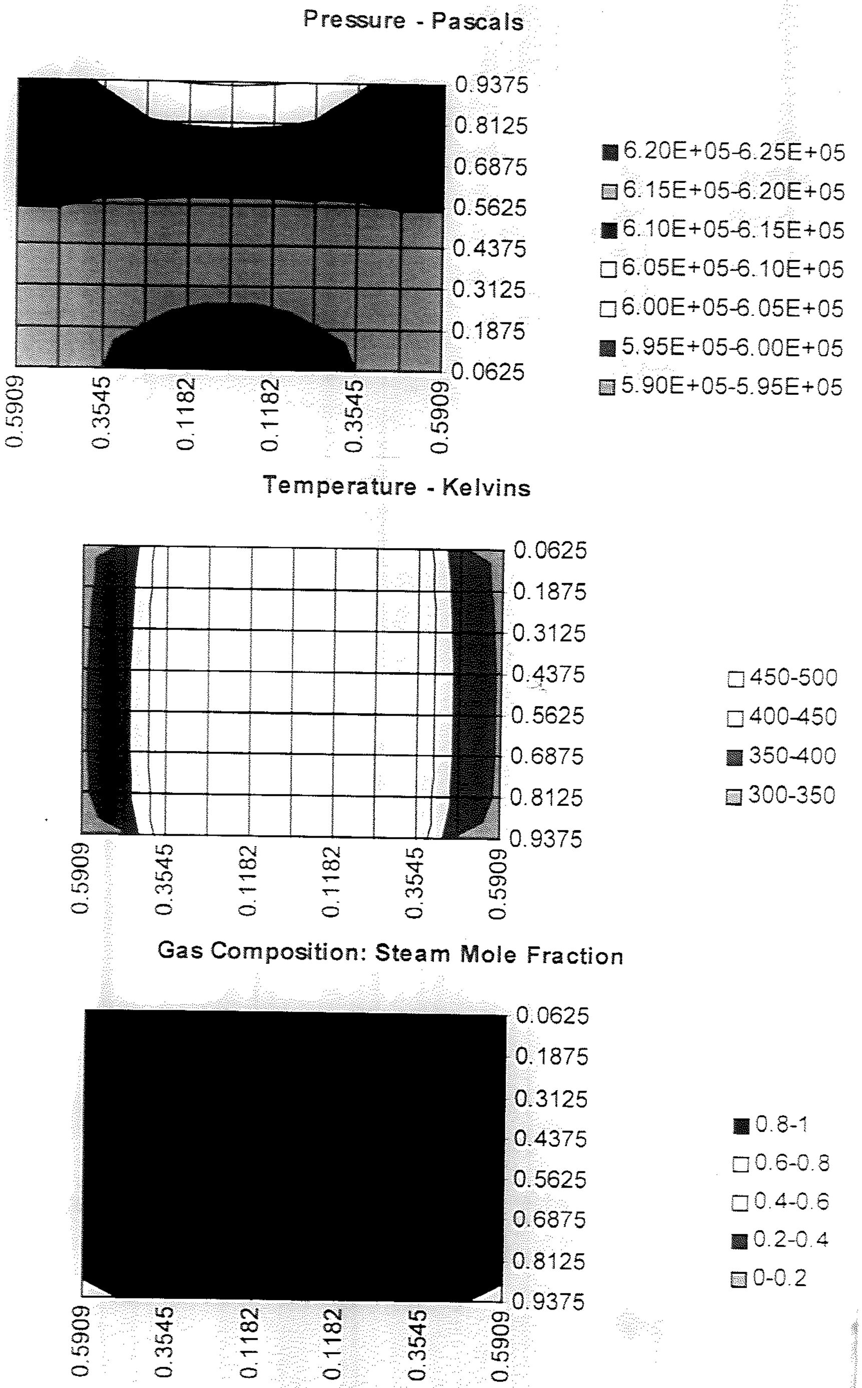

Figure 5.16: Spatial Contours, 1200 seconds.

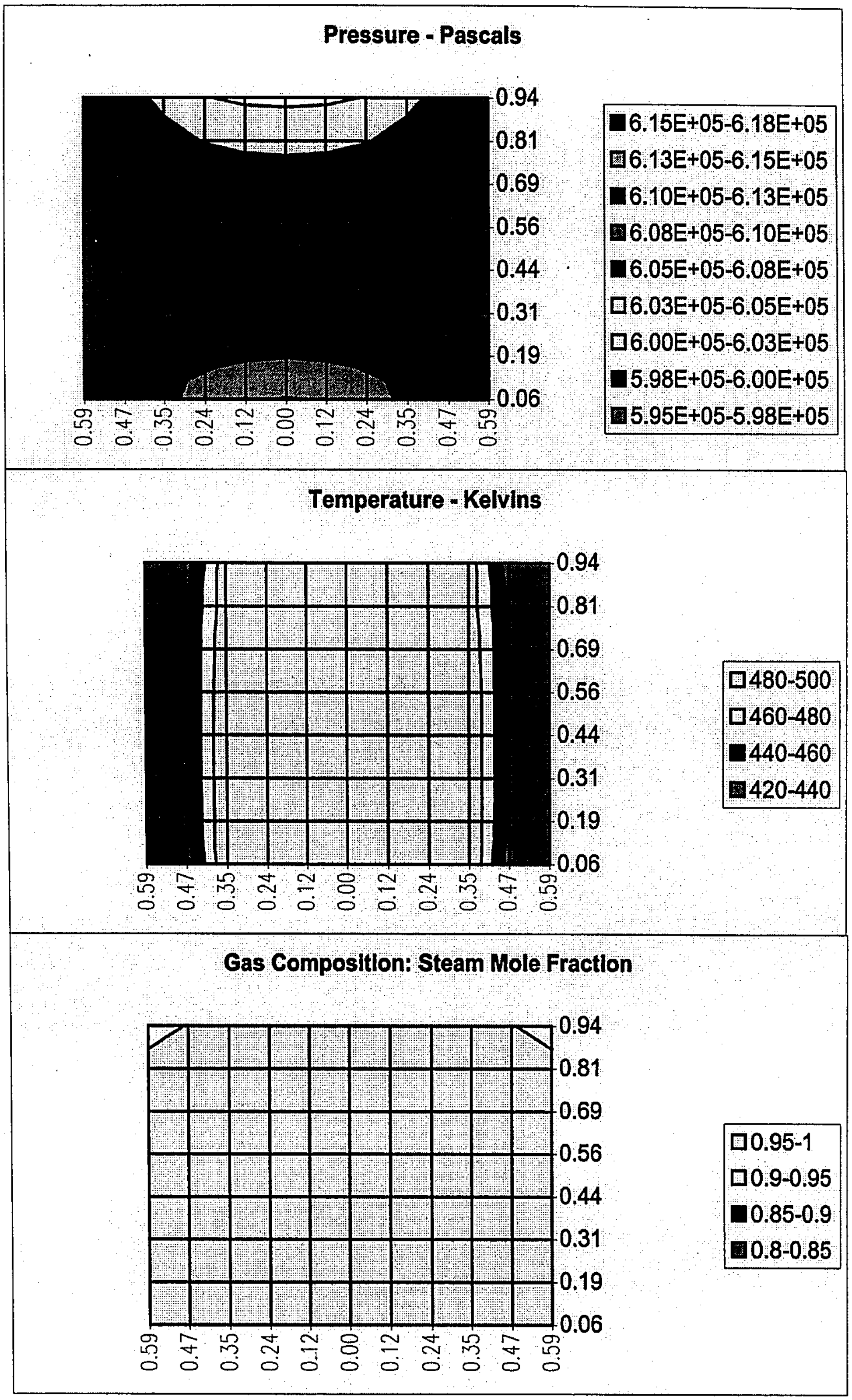

Pressure - Pascals

Temperature - Kelvins

Gas Composition: Steam Mole Fraction

Figure 5.17: Spatial Contours, 9000 seconds.

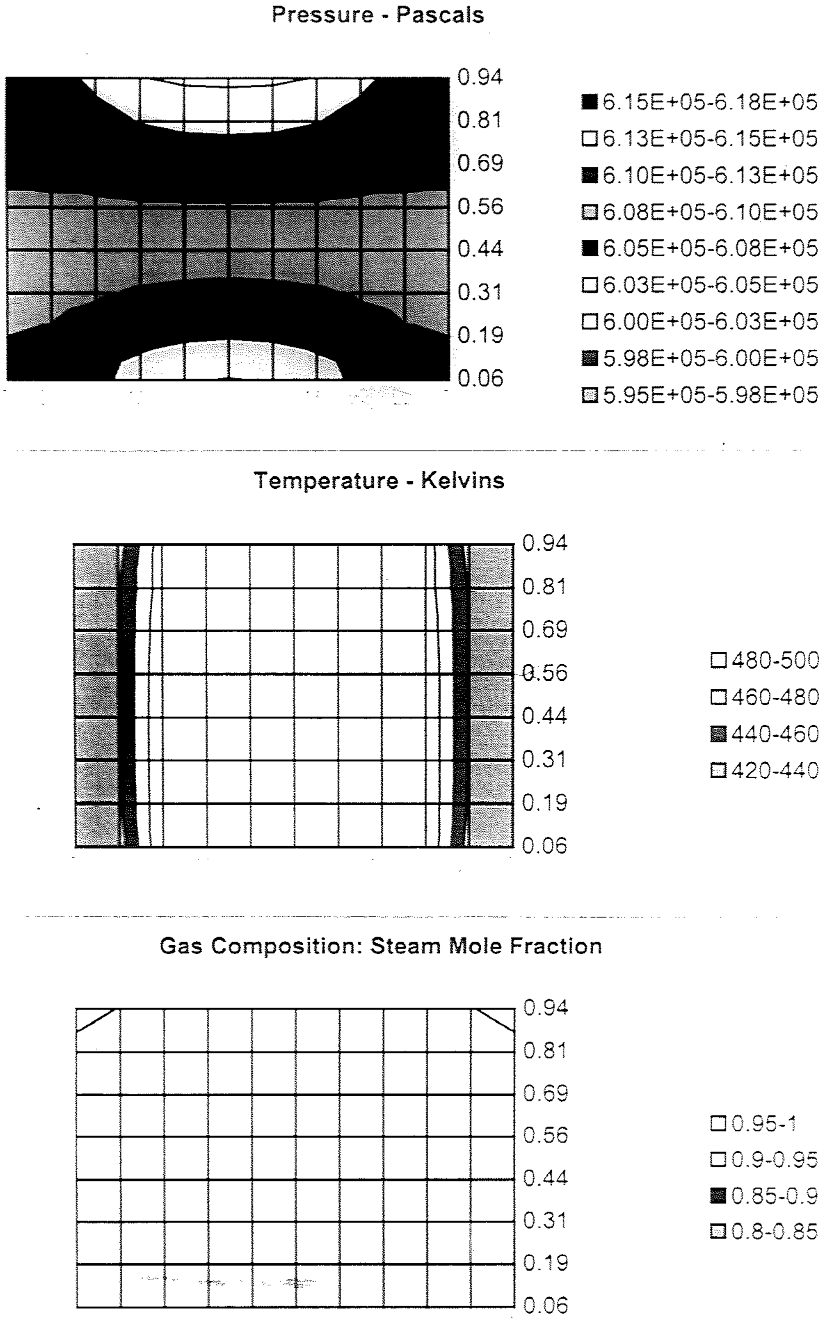

Figure 5.17: Spatial Contours, 9000 seconds.

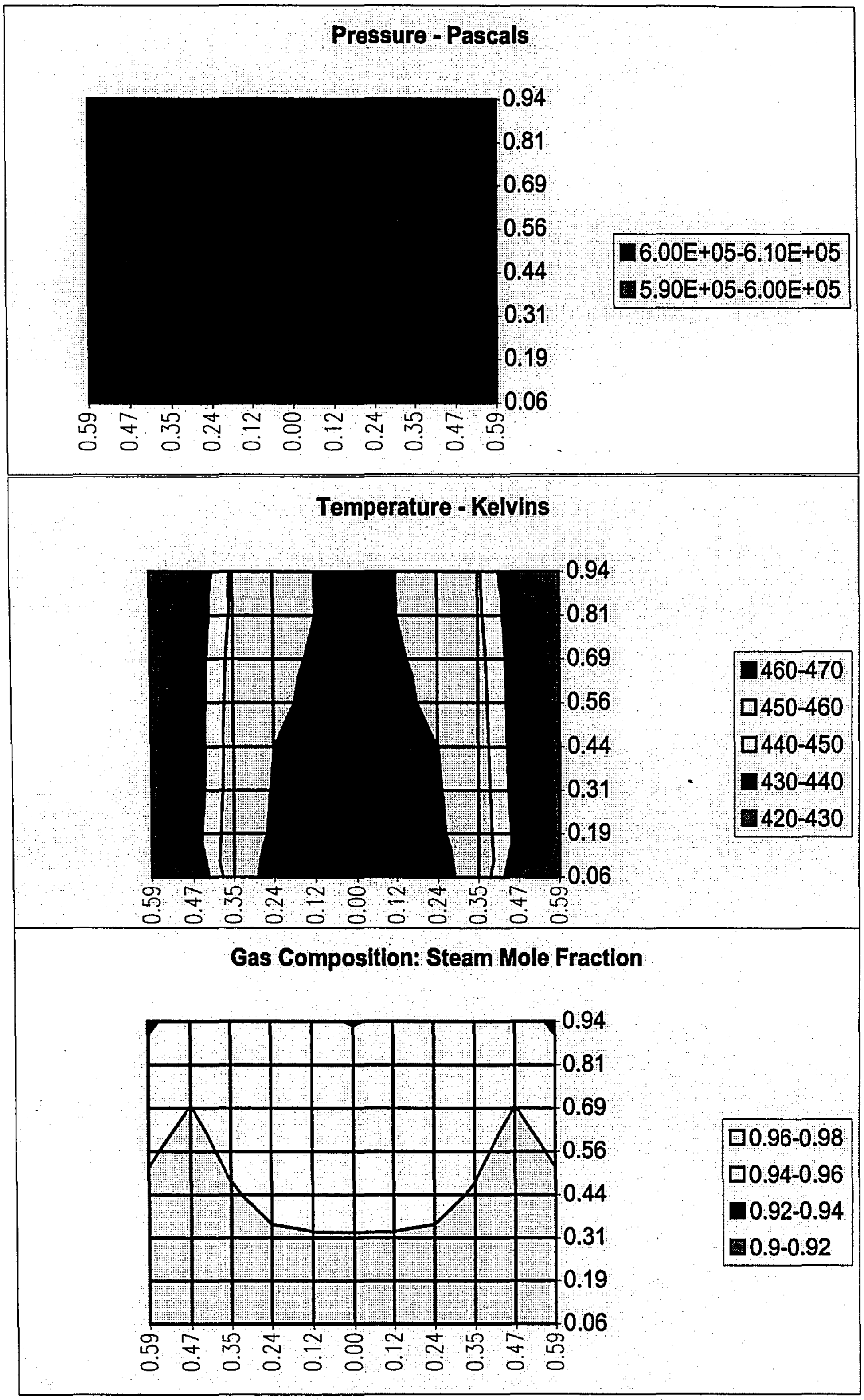
Pressure - Pascals

Temperature - Kelvins

Gas Composition: Steam Mole Fraction

Figure 5.18: Spatial Contours, 12000 seconds.

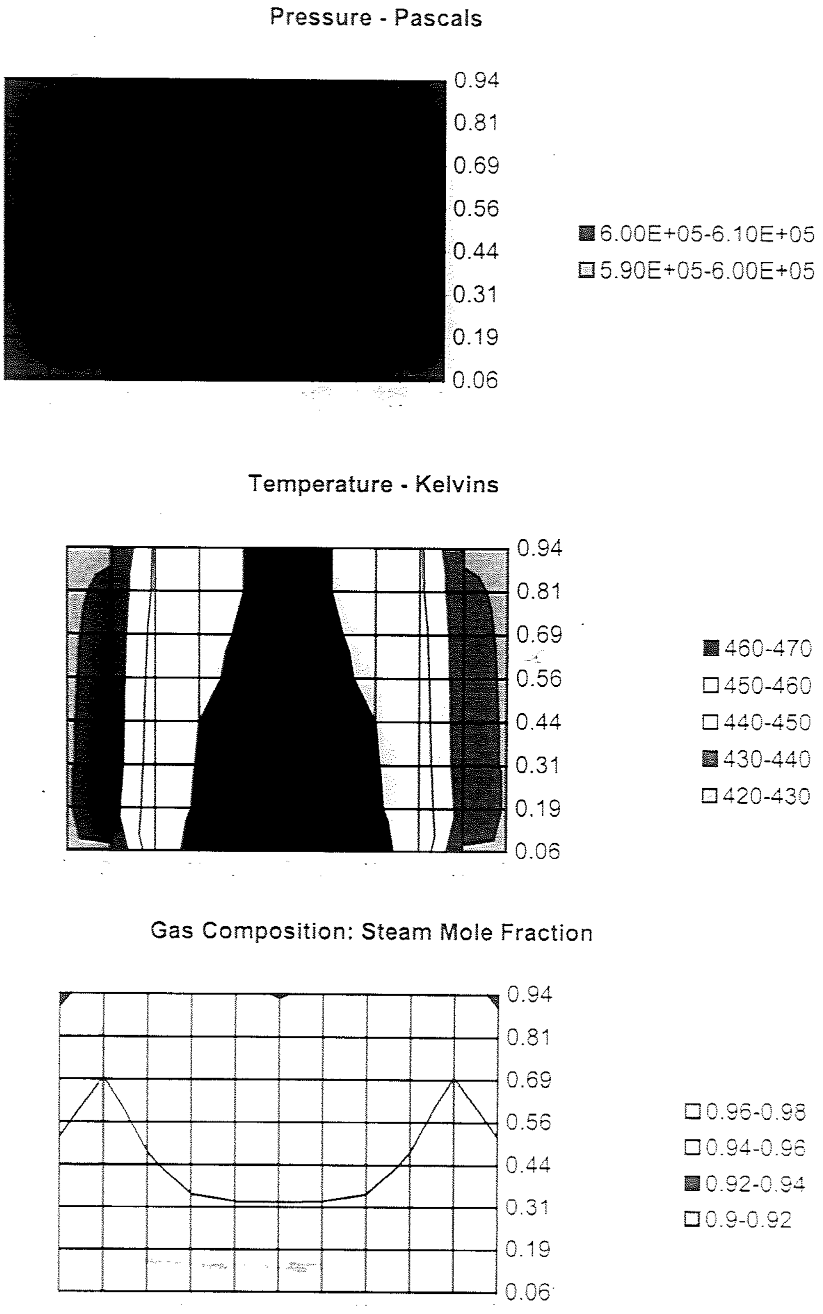

Pressure - Pascals

Temperature - Kelvins

Gas Composition: Steam Mole Fraction

Figure 5.18: Spatial Contours, 12000 seconds.

5.2 Mesh Size Sensitivity

The core-injection simulation was repeated with the spacing halved in both the r- and z-directions for four times as many nodes. That is, the new grid is sixteen vertical by twelve radial positions, for a total of 192 node points.

It is expected that the central difference approximations are on the order of $(\Delta y)^2$, where Δy is the grid spacing. However, the convective upwind-difference term is one-sided, and therefore has accuracy on the order of Δy (it is for this reason that Schiesser and Silebi recommend using multi-point biased upwind differences). The price of increased accuracy through mesh refinement is computational effort, which as described in appendix B, is increased many fold.

The results of this simulation are given in the same order as for the previous two studies, in figures (5.19) through (5.25). In these figures, the results of the "fine" mesh are superimposed on the results of the "coarse" mesh (section 5.1) for direct comparison.

The total computed gas extraction was 2.1% higher for the coarse mesh over the fine, although peak values, in figure (5.19), were higher by 13.7%. The resulting pressure profile, in figure (5.20) was relatively unchanged, as expected, as pressure is a controlled variable.

The simulated temperature transient, figure (5.21), is different between the two cases. The fine mesh case exhibits a slight temperature drop at the beginning

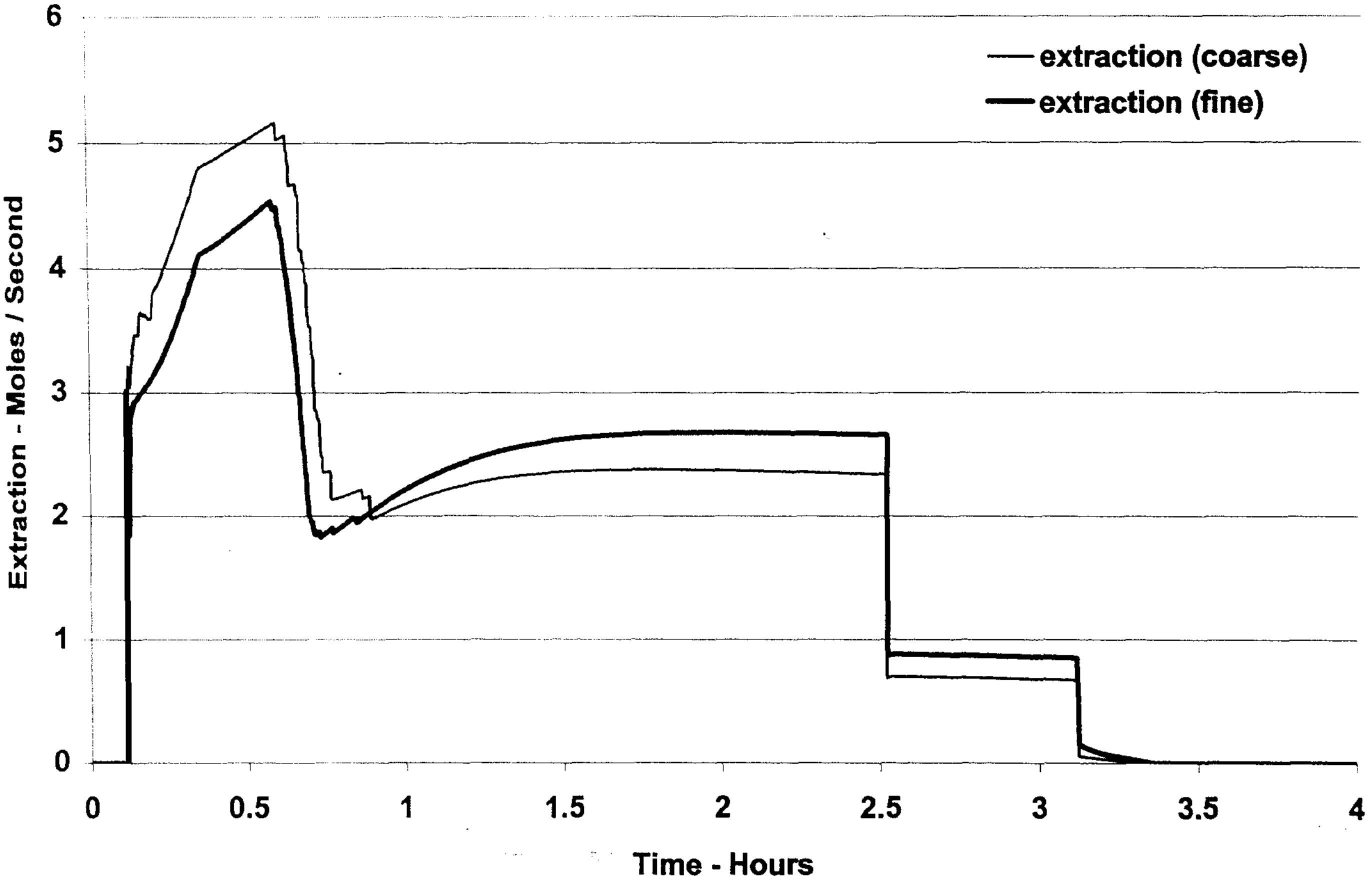

Figure 5.19: Gas Extraction vs. Time (Fine Mesh)

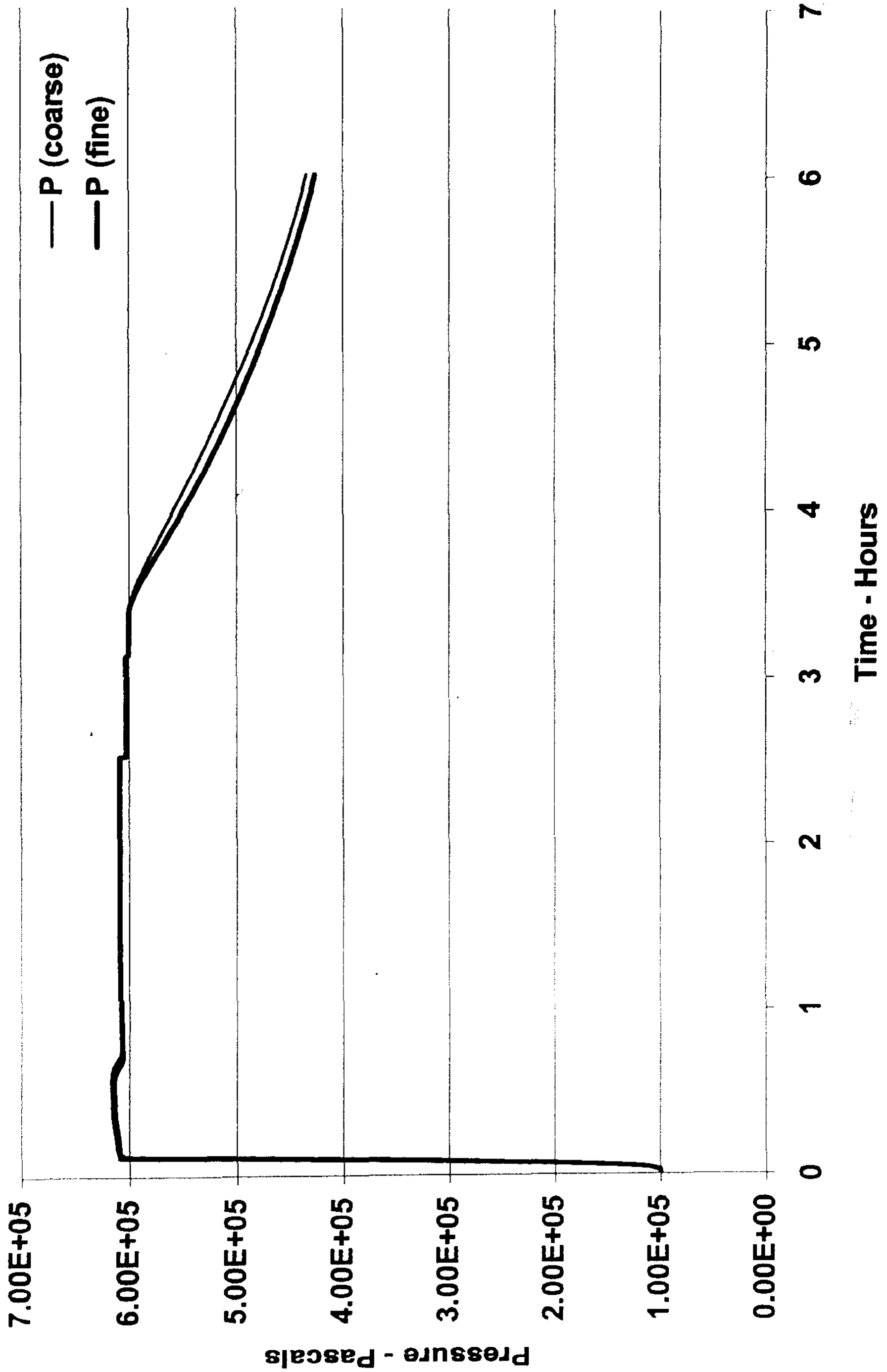

Figure 5.20: Pressure vs. Time (Fine Mesh)

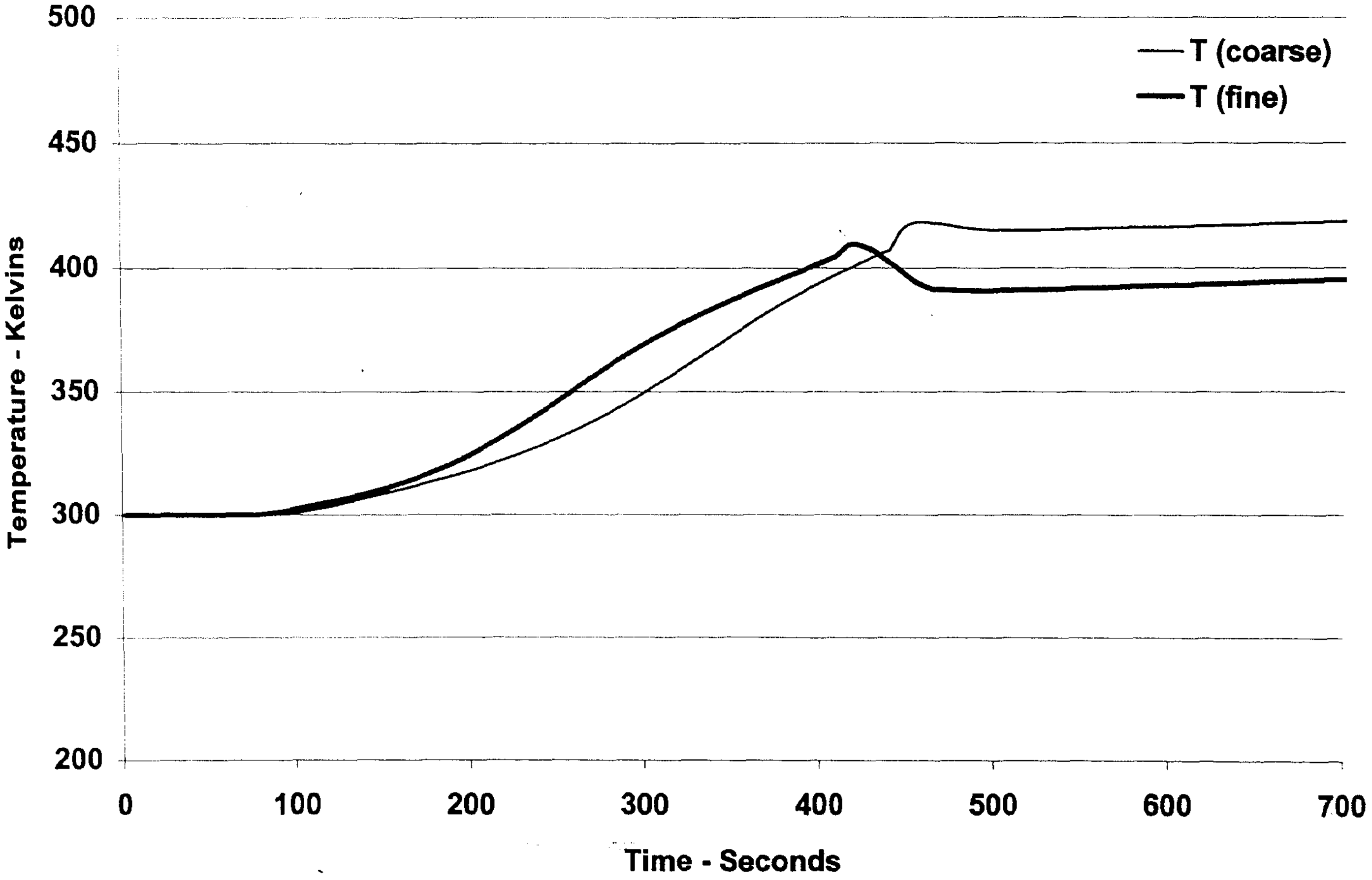

Figure 5.21: Start-up Temperature (Fine Mesh)

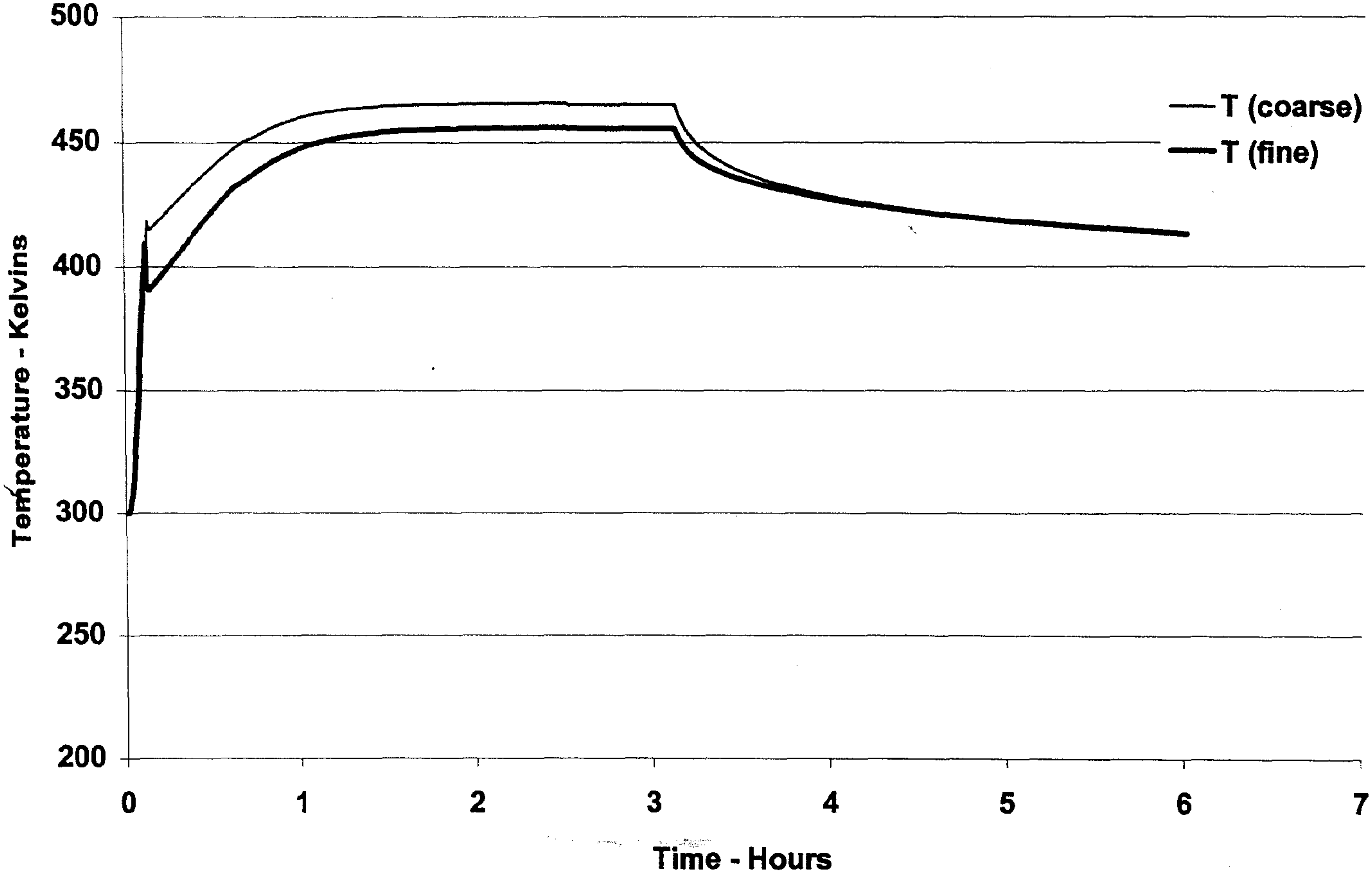

Figure 5.22: Temperature vs. Time (Fine Mesh)

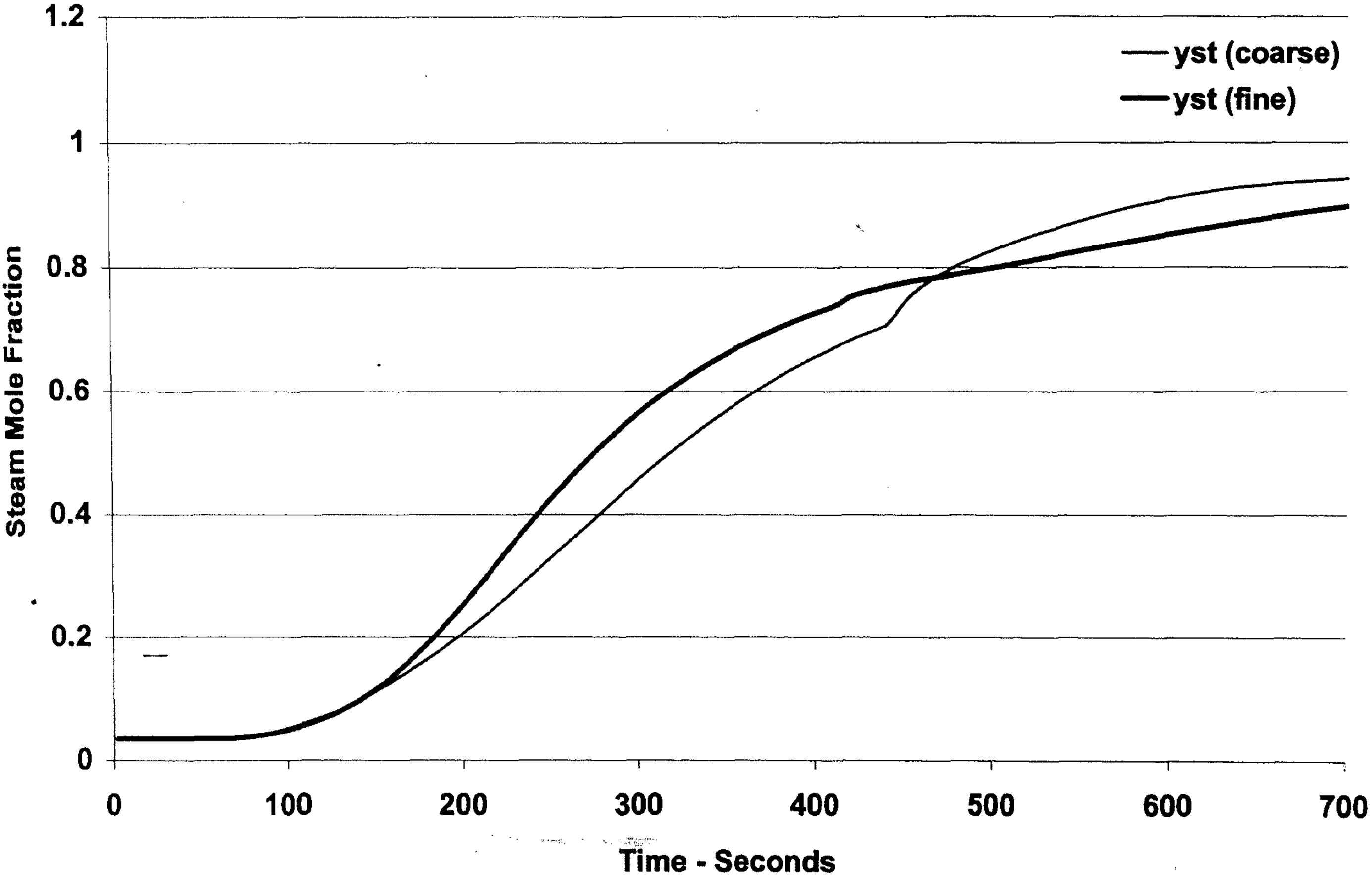

Figure 5.23: Start-up Gas Composition (Fine Mesh)

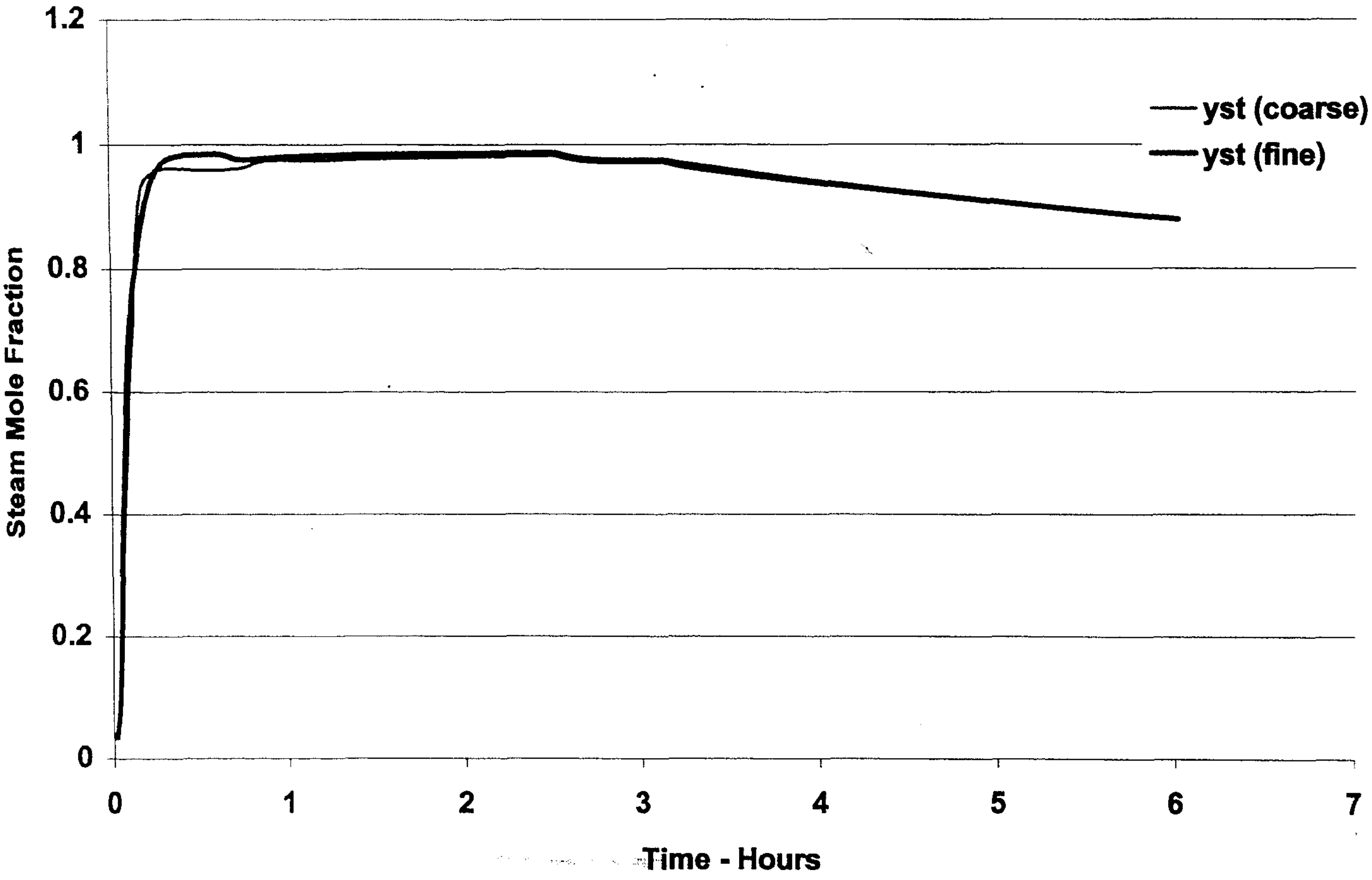

Figure 5.24: Gas Composition vs. Time (Fine Mesh)

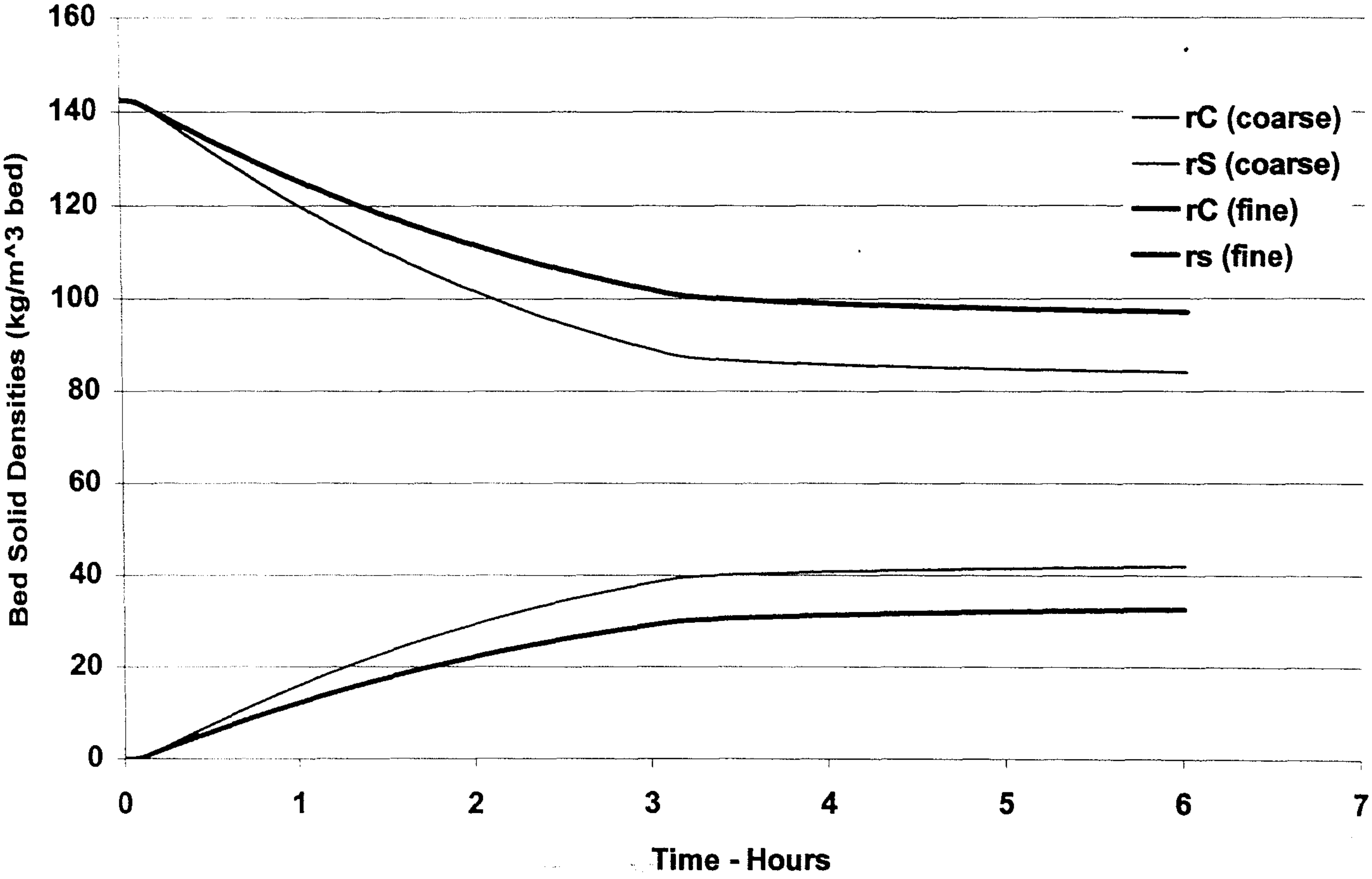

Figure 5.25: Bed Solid Composition vs. Time (Fine Mesh)

of extraction. Overall computed temperatures from the coarse mesh were higher by 11 Kelvins.

The most important result of this is the carbon production, which the coarse mesh computation over-predicts by 28.6%.

The steam concentration histories barely differ between the two cases, although a weaker knee event was exhibited in the transient behavior around extraction point for the fine mesh (figure 5.23).

As in section 5.1.2, intermediate spatial contours are provided in figure (5.26) – (5.29). During the initial transient, in figure (5.26), the fronts are expectedly smoother. Unexpected, though, is the greater depth of penetration of the temperature and steam fronts over the coarse case in figure (5.15). This certainly is in agreement with the higher initial bulk temperatures shown in figure (5.21). Figure (5.27), though, reveals less radial penetration after extraction has started. This is carried through figures (5.28) and (5.29) as well. It is this lower radial penetration which explains the overall temperature deficit in figure (5.22), and hence, the lower carbon production in figure (5.25).

Closer comparison of the contour plots shows that the base of the ‘plume’ is narrower over the injection plane in the fine-mesh simulation. This leads to an approximately 6% decrease in the “effective” injection area (despite the precautions described in section 4.4.1).

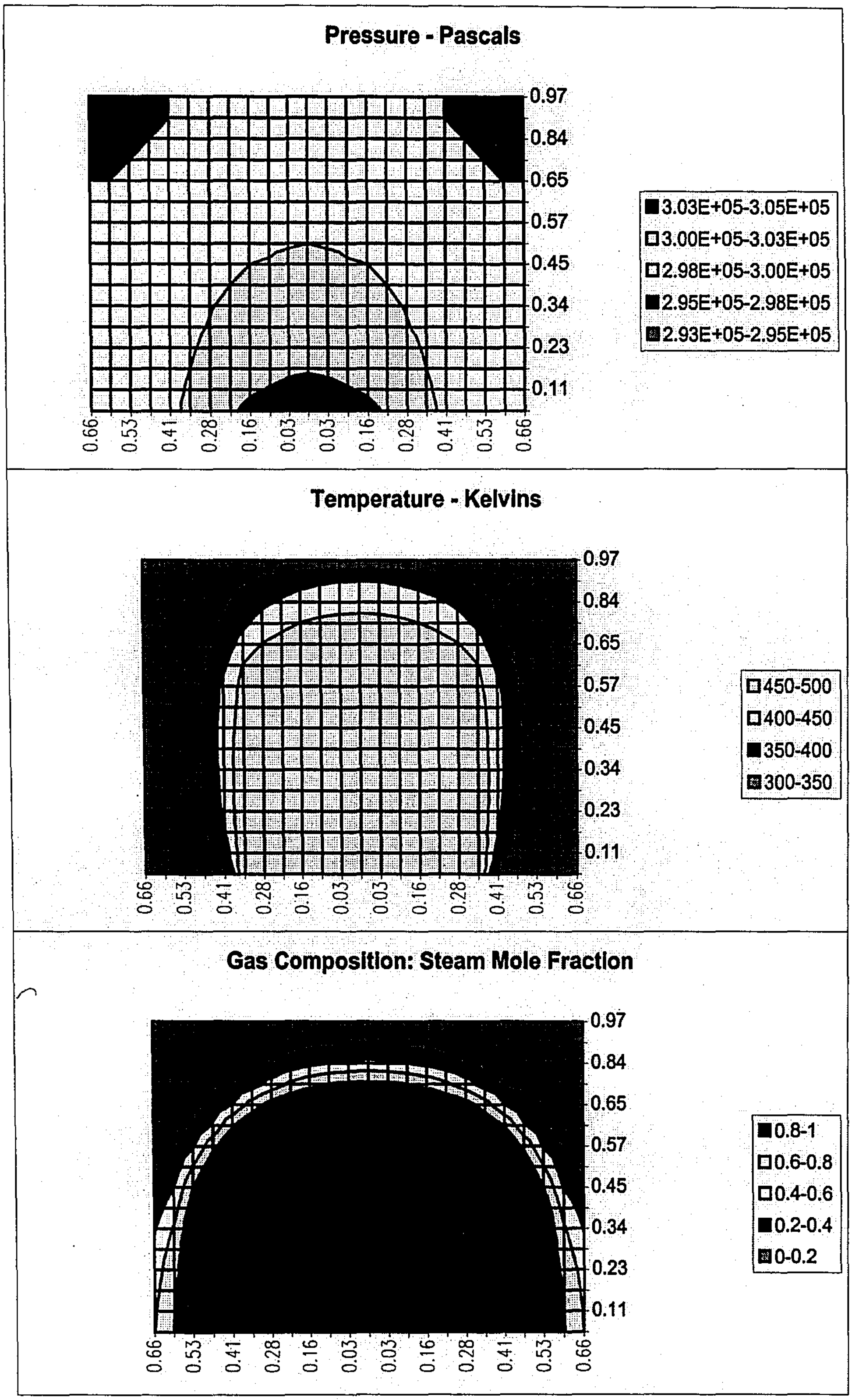

Figure 5.26: Spatial Contours, 300 Seconds (Fine Mesh)

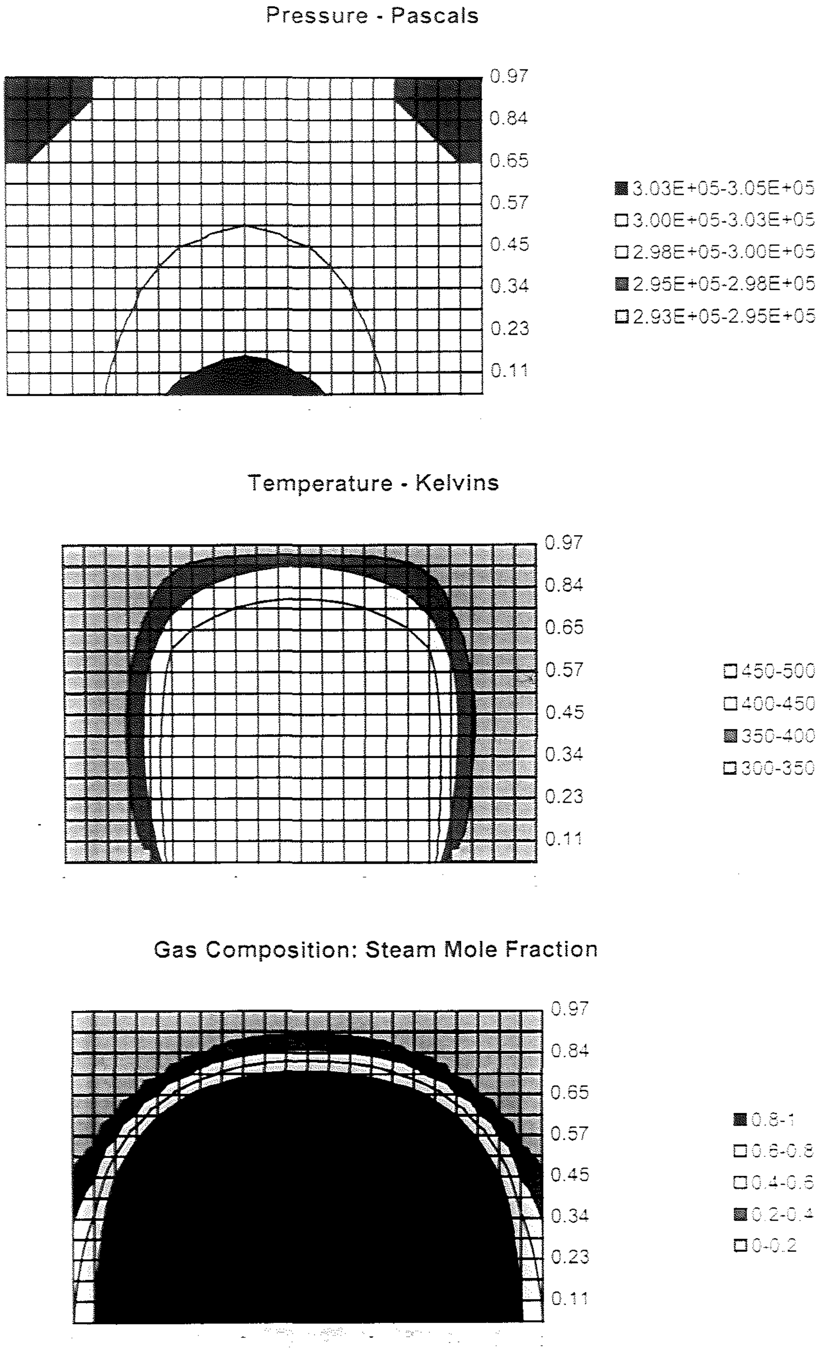

Pressure - Pascals

Temperature - Kelvins

Gas Composition: Steam Mole Fraction

Figure 5.26: Spatial Contours, 300 Seconds (Fine Mesh)

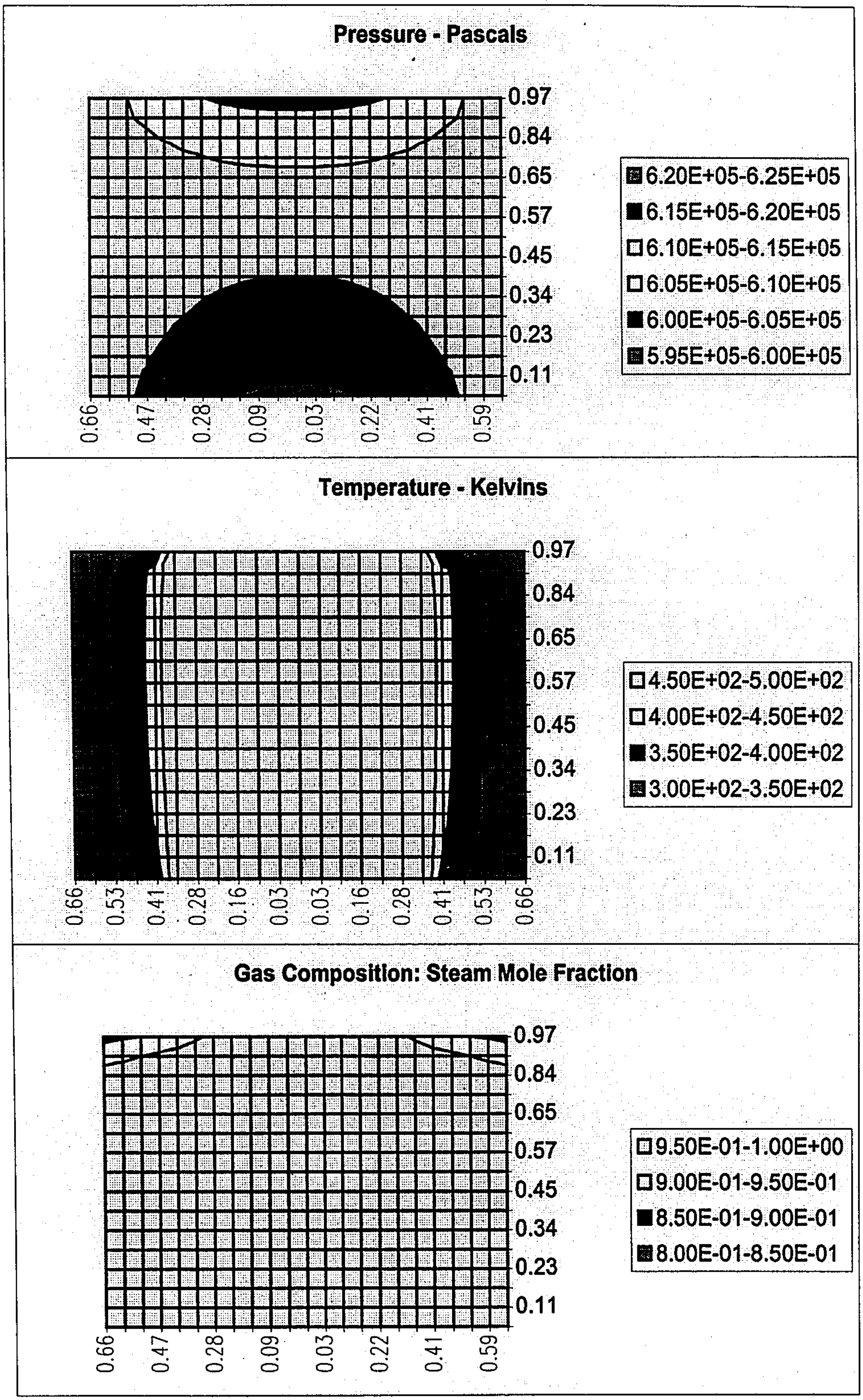

Figure 5.27: Spatial Contours, 1200 Seconds (Fine Mesh)

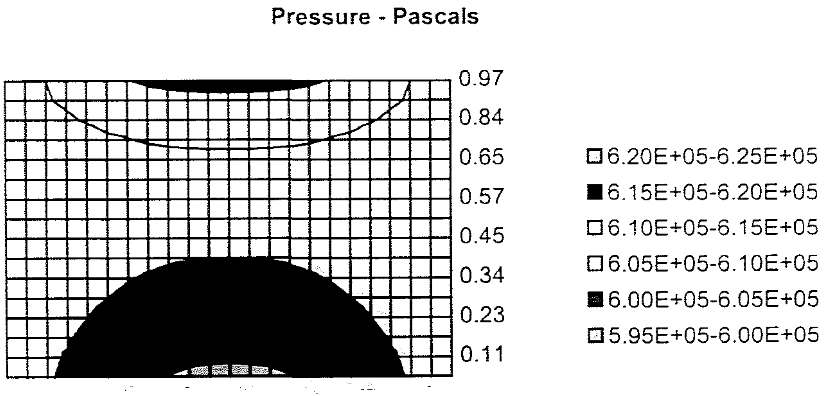

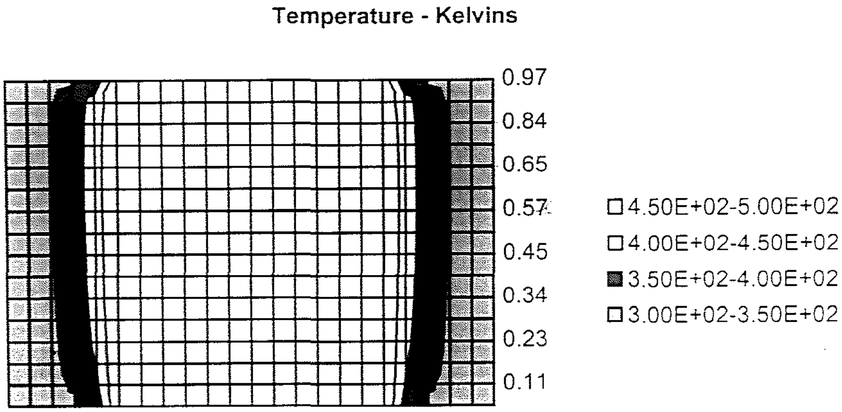

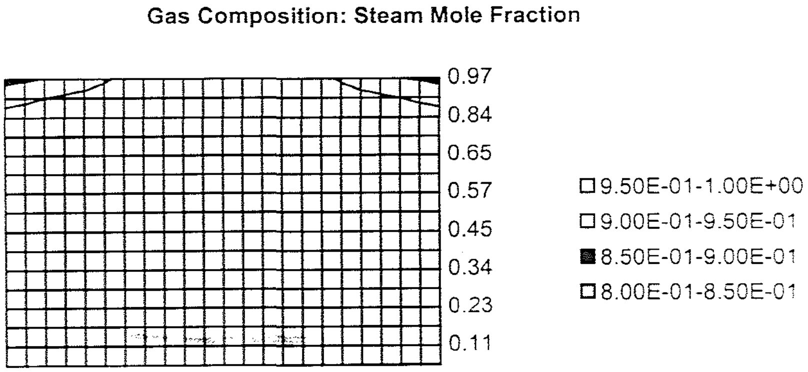

Figure 5.27: Spatial Contours, 1200 Seconds (Fine Mesh)

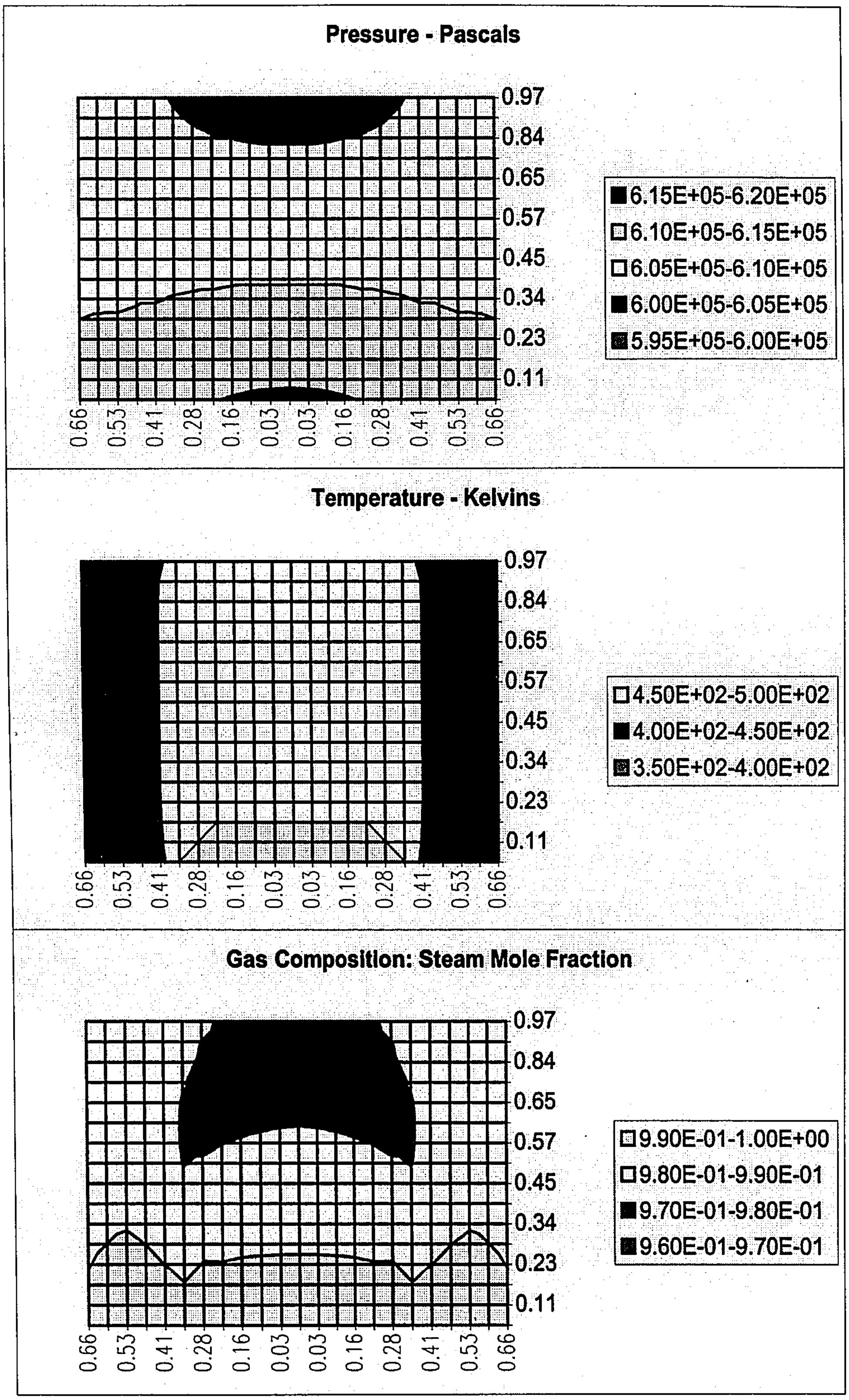

Figure 5.28: Spatial Contours – 9000 Seconds (Fine Mesh)

Pressure - Pascals

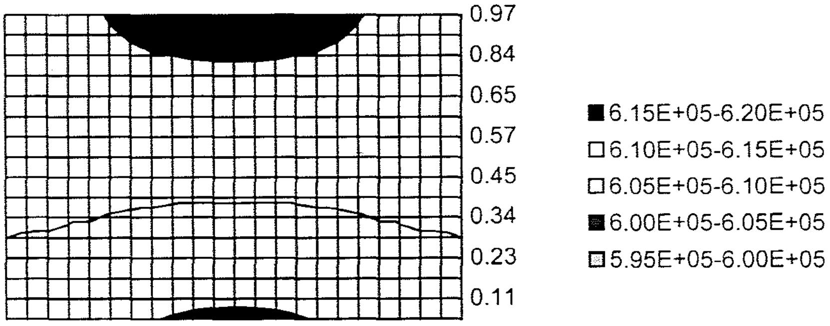

Temperature - Kelvins

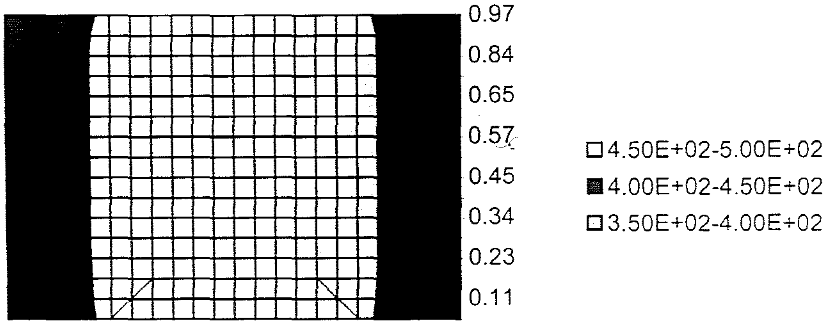

Gas Composition: Steam Mole Fraction

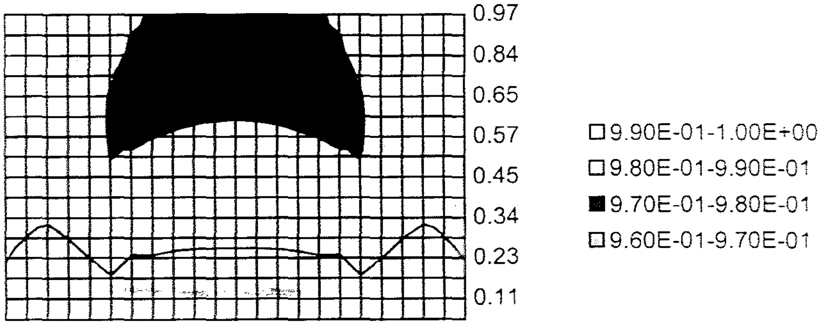

Figure 5.28: Spatial Contours – 9000 Seconds (Fine Mesh)

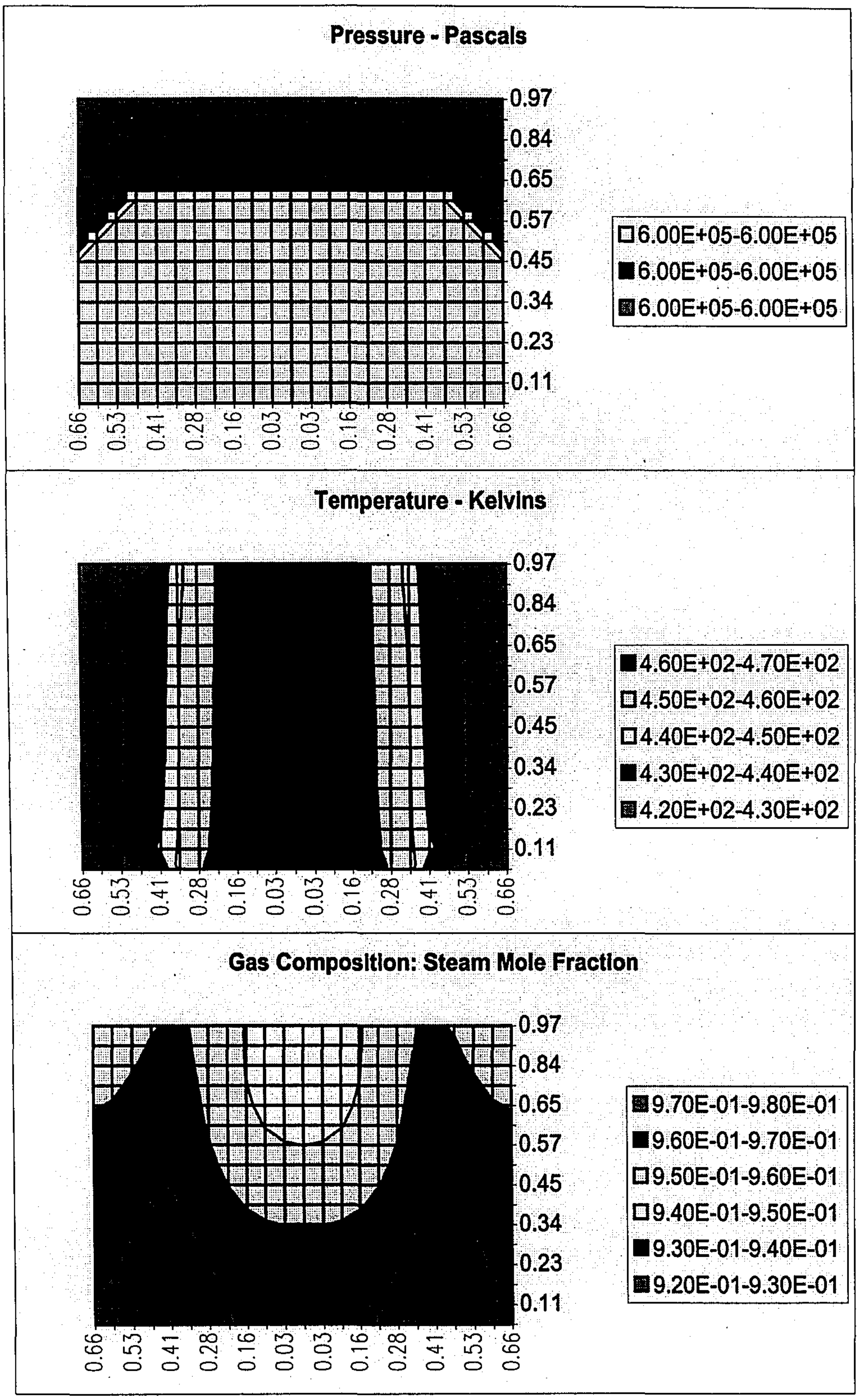

Figure 5.29: Spatial Contours – 12000 Seconds (Fine Mesh)

Pressure - Pascals

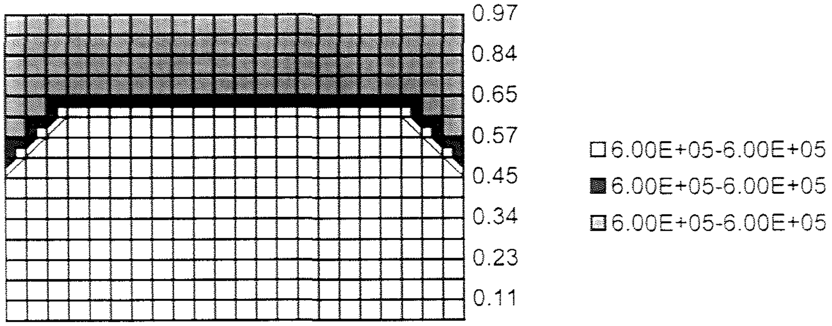

Temperature - Kelvins

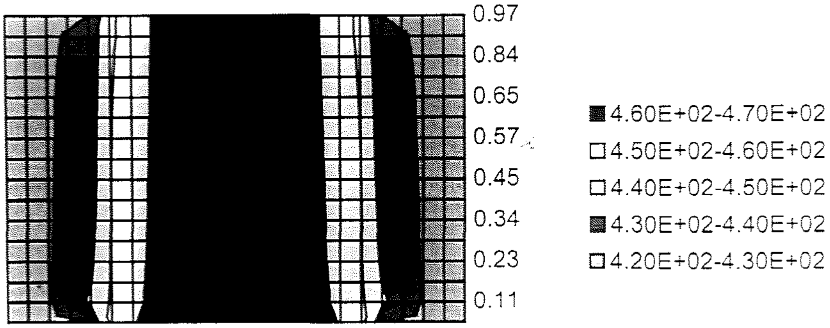

Gas Composition: Steam Mole Fraction

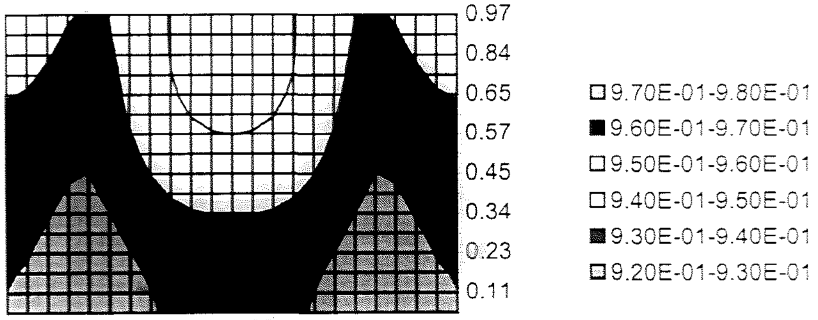

Figure 5.29: Spatial Contours – 12000 Seconds (Fine Mesh)

Given the same flux source term, the result is 6% less simulated steam injection. This may provide an explanation for some of the differences between the results. Further significant refinement of the mesh for sensitivity study was not possible, as the memory demands of the code become too great for a PC.

5.3 Conclusion

Satisfying the conservation equations results in simulated behavior consistent with that of a packed-bed reactor. These equations can be solved using the Numerical Method of Lines. However, successful solution requires the use of upwind differences of the convected quantities. The desired accuracy of the results must be balanced with the computational demands of the code, which may be severe for three-dimensional problems.

The resulting code is sufficient to determine the dynamic characteristics of the system investigated. This will be the basis for a future extension to include a vapor headspace feature, as well as other refinements.

5.4 Future Work

Before the model is used as a design tool, further refinements need to be made. The thermodynamics of the liquid-vapor system need to be modeled with more rigor, taking into account the nonidealities of steam [11], [19]. Further, other thermophysical properties such as viscosity and noncondensible gas heat capacity should be modeled with proper temperature dependence [10]. Last, proper description of the bed transport quantities (e.g., permeability, conductivity, binary gas diffusivity) should be completely described using established empirical relationships.

The next stage of realism in the model will be proper characterization of the vapor space that in the physical reactor exists above the bed. This feature may require treatment of a moving boundary.

Before any complexities are added to the model, however, the numerical difficulties and tradeoffs between coarse and fine grid spacing must ultimately be reduced by using either an adaptive mesh routine or higher-order derivative approximations [16].

References

1. Wakao, N., Kaguei, S., Heat and Mass Transfer in Packed Beds, Gordon and Breach Science Publishers, New York, 1982
2. Thorsness, C. B., Kang, S. W., A Method-of-Line Approach to Solution of Packed-Bed Flow Problems Related to Underground Coal Gasification Process, Lawrence Livermore National Laboratory Report UCRL-90731, 1984
3. Thorsness, C. B., Kang, S. W., Further Development of a General-Purpose, Packed-Bed Model for Analysis of Underground Coal Gasification Process, Lawrence Livermore National Laboratory Report UCRL-92489, 1985
4. Thorsness, C. B., Process Modeling of Hydrothermal Treatment of Municipal Solid Waste to form High Solids Slurries in a Pilot Scale System, Lawrence Livermore National Laboratory Report UCRL-ID-119685, 1995
5. Thorsness, C. B., A Multidimensional Model of Direct-Steam Heating of Newspaper and Municipal Solid Waste in a Hydrothermal Reactor, Lawrence Livermore National Laboratory Report UCRL-ID-228576, 1996
6. Johnson, S. H., Hindmarsh, A. C., Unpublished Work: MSH Code, Livermore, California, 1996
7. Bird, Stewart, Lightfoot, Transport Phenomena, John Wiley and Sons, New York, 1960

8. Silebi, C. A., Schiesser, W. E., Dynamic Modeling of Transport Process Systems, Academic Press, San Diego, 1992

9. Incorpera, F. P., De Witt, D. P., Fundamentals of Heat and Mass Transfer, 3rd Ed., John Wiley & Sons, New York, 1990

10. Cengel, Y. A., Boles, M. A., Thermodynamics, An Engineering Approach, 2nd Ed., McGraw-Hill, Inc., New York, 1994

11. Prausnitz, J. M., et. al., Molecular Thermodynamics of Fluid-Phase Equilibria, 2nd Ed., Prentice Hall, New Jersey, 07632

12. Luyben, W., Process Modeling, Simulation and Control for Chemical Engineers, McGraw-Hill, Inc., New York, 1990

13. Schiesser, W. E., The Numerical Method of Lines Integration of Partial Differential Equations, Academic Press, San Diego, 1991

14. Panton, R. L., Incompressible Flow, John Wiley & Sons, New York, 1984

15. Press, W. H., et. al., Numerical Recipes in FORTRAN, The Art of Scientific Computing, 2nd Ed., Cambridge University Press, 1992

16. Schiesser, W. E., and Silebi, C. A., Computational Transport Phenomena, Cambridge University Press, 1997

17. Patankar, S. V., Numerical Heat Transfer and Fluid Flow, Hemisphere Series on Computational Methods in Mechanics and Thermal Science, 1980

18. Petzold, L. R, A Description of DASSL: A Differential/Algebraic System Solver, Scientific Computing, R. S. Stepleman et al., eds., North-Holland, Amsterdam, 1983

19. Tong, L. S., and Tang, Y. S., Boiling Heat Transfer and Two-Phase Flow, 2nd Ed., Taylor & Francis, 1997

20. Van de Wouwer, A., Sauces, P., and Schiesser, W. E., Some User-oriented Comparisons of Adaptive Grid Methods for Partial Differential Equations in One Space Dimension, Applied Numerical Mathematics, 26, 1998

Appendix A

Thermophysical Properties

Bed Characteristics and General Constants:

P_{inf}	$1x10^{5}$	Nominal Pressure, Pa
T_{inf}	300	Nominal Temperature, K
T_{ref}	298	Reference State Temperature, K
R	8.314	Universal Gas Constant, Pa m^3/mol K
g	9.81	Gravitational Acceleration, m/s^2
ϕ^0	0.5	Internal Void Fraction of Solid Particle
D	$0.144x10^{-4}$	Effective Gas Dispersion, m^2/s
P_{cap}^{0}	1.0d5	Intrinsic Capillary Pressure, Pa
Γ^0	$5x10^{-12}$	Intrinsic Bed Permeability m^2
h_{wall}	0	Interior Wall Convection, W/m^2K
K_{mt}	$1x10^{-6}$	VLE Mass Transfer Coeff., mol/(Pa s m^3)

Solid Species Properties:

ρ_s^0	1000	Intrinsic Solid Density, kg/m^3
Cp_s	1x10+3	Solid Specific Heat, J/kg K
$h_{f,s}^{0}$	$-42x10^{3}$	Solid Enthalpy of Formation at 298K, J/mol
k_{sol}	0.5	Solid Thermal Conductivity, W/(m K)
A	$6.3x10^{4}$	Arrhenius Constant, 1/s
α_s	1	Solid Reactant Stoich. Coeff., kg/kg
T_a	$1x10^{4}$	Activation Temperature, K

ρ_c^0	1000	Intrinsic Carbon Density, kg/m^3
α_c	0.72	Carbon Product Stoich. Coeff., kg/kg
Cp_c	1x10+3	Carbon Thermal Conductivity, W/m K
$h_{f,c}^{0}$	$-42x10^{3}$	Carbon Heat of Formation at 298K

Liquid Water Properties:

ρ_w^0	880	Intrinsic Density of Liquid Water
α_w	10.56	Water Stoich. Coeff., mol/kg
MW_w	$18x10^{-3}$	Molecular Weight of Water, kg/mol
μ_w	$2110x10^{-7}$	Viscosity of Liquid Water, Pa s
$h_{f,lw}^{0}$	$2.8583x10^{5}$	Liq. Enthalpy of Formation at 298K, J/mol

h_{lw}^{0}	104.89	Liquid Enthalpy at 298K, J/mol
Cp_{lw}	76	Liquid Specific Heat, J/mol K
Klw	0.8	Liquid Thermal Conductivity, W/m^{2}

Cp_{st}	33.67	Steam Heat Capacity, J/(mol-K)
h_{fst}^{0}	-2.418×10^{5}	Steam Enthalpy of Formation at 298K, J/mol
h_{st}^{0}	9904	Steam Enthalpy at 298K, J/mol
P_e	8.8888×10^{10}	Saturation Pressure Constant T<410K
P_e	2.9929×10^{10}	Saturation Pressure Constant T>410K
a_e	5114.	Saturation Temp. Constant T<410K
a_e	4666.3	Saturation Temp. Constant T<410K

α_{ng}	2.38	Noncondensible Stoich. Coeff., mol/kg
Cp_{ng}	30.1	Noncondensible Gas Specific Heat, J/(mol K)
$h_{f,ng}^{0}$	0	Noncon. Gas Enthalpy of Formation at 298K, J/mol
h_{ng}^{0}	8.669×10^{3}	Noncondensible Gas Enthalpy at 298K, J/mol
μ_{gas}	12.9×10^{6}	Gas Viscosity, Pa-sec
k_{gas}	0.05	Gas Thermal Conductivity watts/(m-K)

Appendix B

Computational Performance Measures

Charts indicating the relative computational effort of the code for the three simulations studied are included in this appendix. Figure (A.1) indicates the number of steps taken by the integrator per unit time. Figure (A.2) charts the number of right hand side evaluations by the code, and Figure (A.3) shows the number of Jacobian evaluations performed. In order to more clearly illustrate the computational effort required by finer mesh definition, Figure (A.4) describes the total number of right hand side evaluations performed, times the number of grid points for which the calculations are performed. This, in essence, is an indicator of the total number of times the governing equations are evaluated by the code.

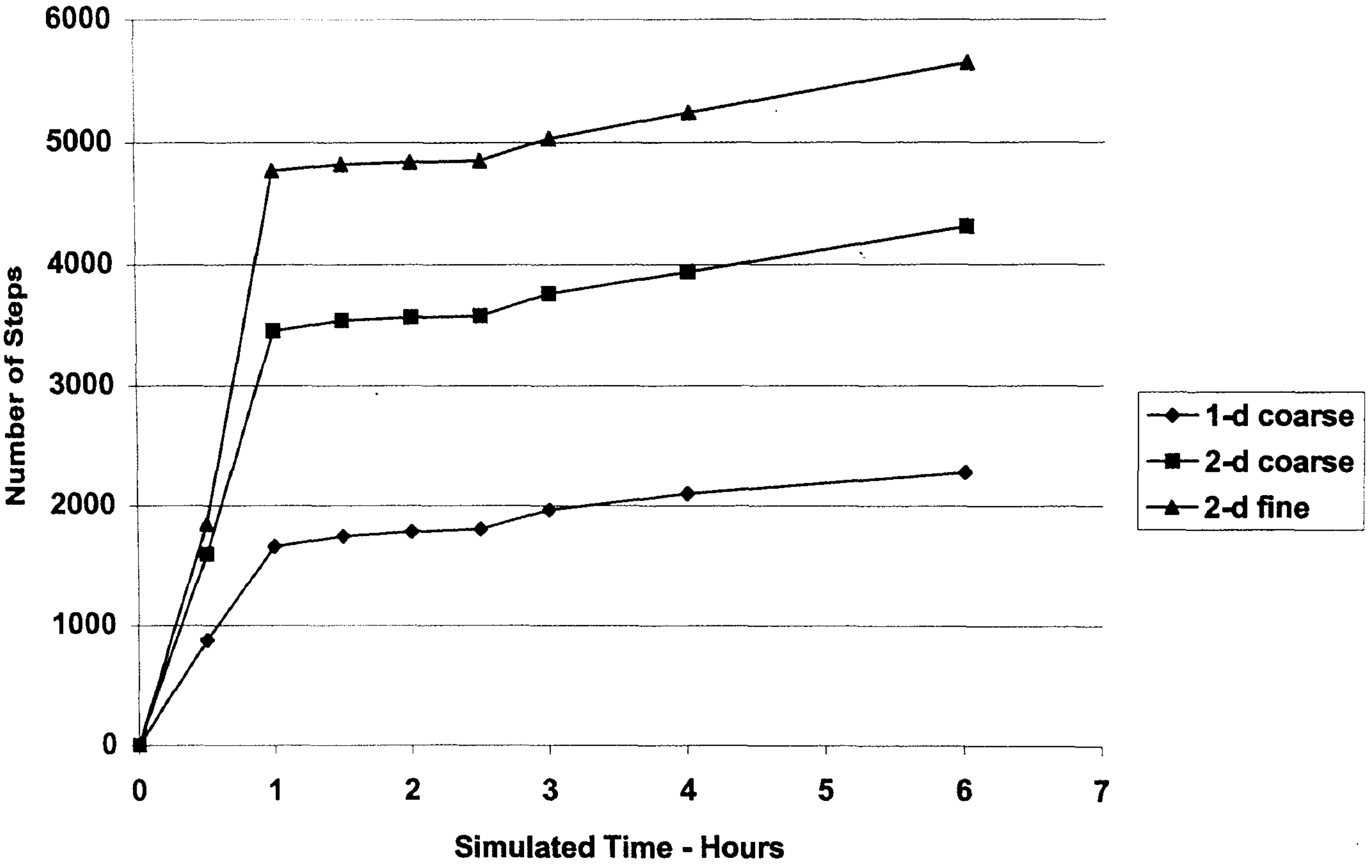

Figure B.1: Number of Integrator Steps vs. Simulated Time

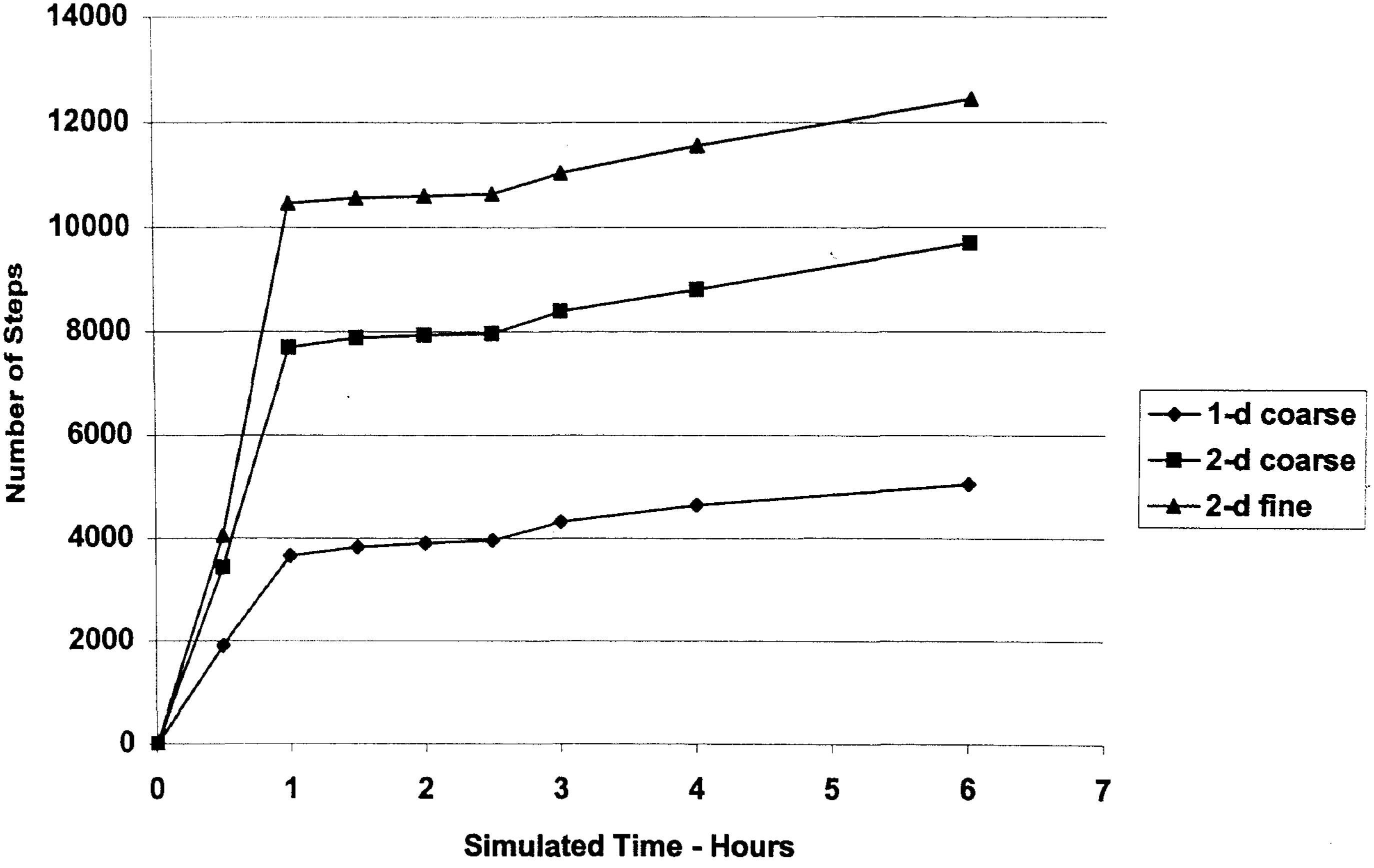

Figure B.2: Number of RHS Evaluations vs. Simulated Time

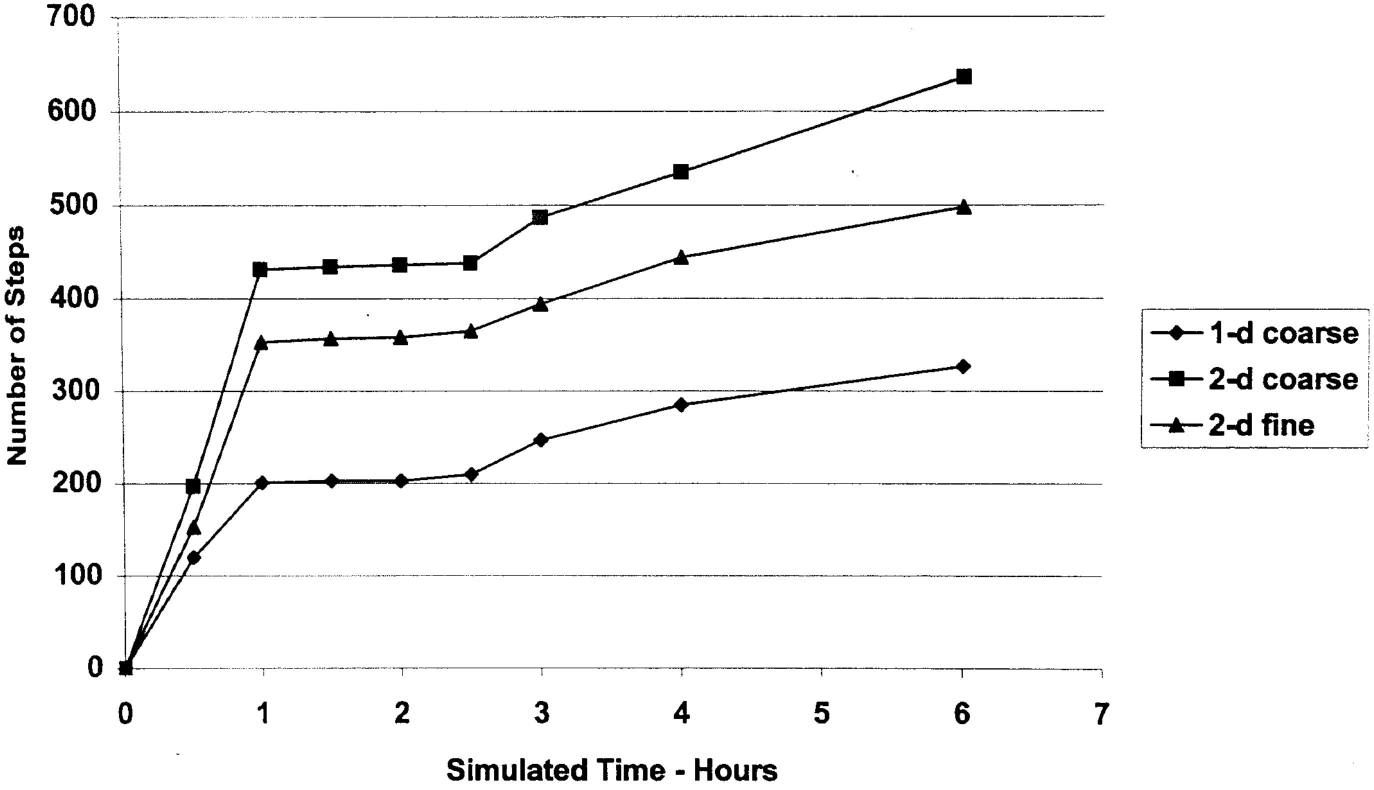

Figure B.3: Number of Jacobian Evaluations vs. Simulated Time

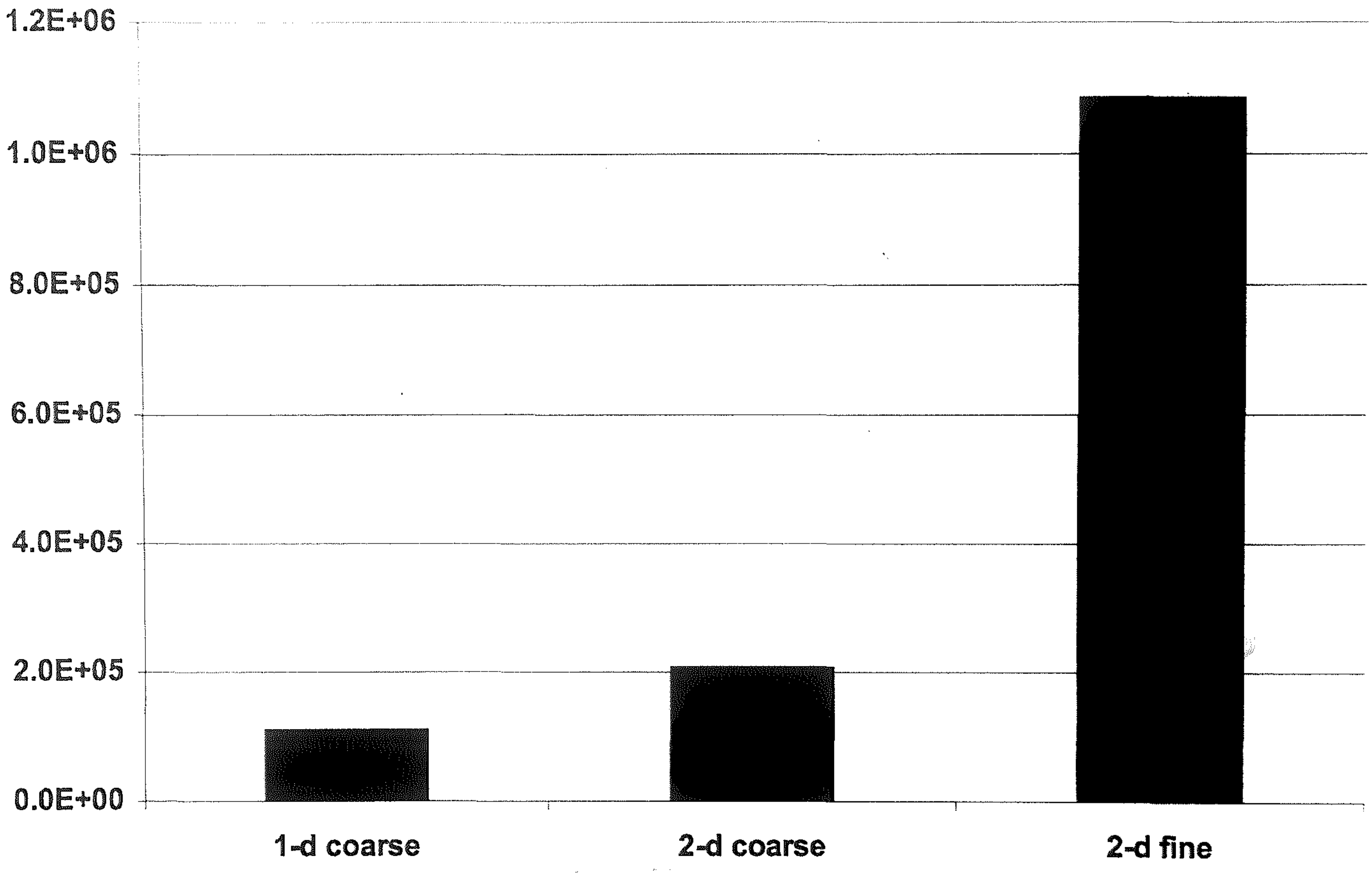

Figure B.4: Total RHS Evaluations Times Number of Grid Points

Vita

Steven Quintavalla was born in New York, New York, in 1972. His parents, Paul and Jeanne Quintavalla, are also natives of New York. He received a bachelor of science degree in mechanical engineering from Rutgers University College of Engineering in 1995, and is currently attending Lehigh University for graduate studies. He currently holds a position as research engineer at the United States Golf Association Research & Test Center. Mr. Quintavalla has one patent pending.

END
OF
TITLE